# Biglobal resolvent analysis of separated flow over a NACA0012 airfoil

Laura Victoria Rolandi , Luke Smith , Michael Amitay , Vassilis Theofilis , and Kunihiko Taira

Corresponding author: Laura Victoria Rolandi, vrolandi@g.ucla.edu

(Received 4 January 2025; revised 3 September 2025; accepted 17 September 2025)

The effects of Reynolds number across Re = 1000, 2500, 5000 and 10000 on separated flow over a two-dimensional NACA0012 airfoil at an angle of attack of  $\alpha = 14^{\circ}$ are investigated through biglobal resolvent analysis. We identify modal structures and energy amplifications over a range of frequencies, spanwise wavenumbers, and values of the discount parameter, providing insights across various time scales. Using temporal discounting, we find that the shear-layer dynamics dominates over short time horizons, while the wake dynamics becomes the primary amplification mechanism over long time horizons. Spanwise effects also appear over long time horizons, sustained by low frequencies. The low-frequency and high-wavenumber structures are found to be dominated by elliptic mechanisms within the recirculation region. At a fixed angle of attack and across the Reynolds numbers, the response modes shift from wake-dominated structures at low frequencies to shear-layer-dominated structures at higher frequencies. The frequency at which the dominant mechanism changes is independent of the Reynolds number. Comparisons at a different angle of attack ( $\alpha = 9^{\circ}$ ) show that the transition from wake to shear-layer dynamics with increasing frequency only occurs if the unsteady flow is three-dimensional. We also study the dominant frequencies associated with wake and shear-layer dynamics across the angles of attack and Reynolds numbers, and confirm characteristic scaling laws from the literature.

**Key words:** separated flows, transition to turbulence, instability

<sup>&</sup>lt;sup>1</sup>Department of Mechanical and Aerospace Engineering, University of California, Los Angeles, CA 90095, USA

<sup>&</sup>lt;sup>2</sup>Department of Mechanical, Aerospace and Nuclear Engineering, Rensselaer Polytechnic Institute, Troy, NY 12180, USA

<sup>&</sup>lt;sup>3</sup>Faculty of Aerospace Engineering, Israel Institute of Technology, Haifa 32000, Israel

#### 1. Introduction

Understanding and controlling separated flows is important for improving performance of a range of fluid-based systems. Flow separation over a wing can significantly reduce lift and increase drag, leading to diminished aerodynamic efficiency and higher fuel consumption. This issue impacts not only aerodynamic performance but also affects stability and control of the air vehicle, which can compromise its overall safety and the operational effectiveness.

A helpful tool for the design of flow separation control strategies is resolvent analysis (Trefethen *et al.* 1993; Jovanović & Bamieh 2005), which helps us to understand the flow characteristics by linearizing the governing equations around a base flow, modelling the nonlinear terms as an external forcing (McKeon & Sharma 2010) and transforming the dynamics into an input—output problem (Jovanović 2021). The use of the time-averaged flow as the base flow, with the assumption of statistical stationarity, allows for the extension of resolvent analysis to turbulent flows (McKeon & Sharma 2010; Towne, Schmidt & Colonius 2018; Yeh & Taira 2019; Martini *et al.* 2020).

With resolvent analysis, complex flow fields are decomposed into coherent modal structures at all frequencies. These modal structures are the optimal pair of forcing and response modes, with corresponding gain quantifying the energy amplification. By studying this decomposition, is possible to identify the dominant mechanisms that drive the dynamics of the flow.

Resolvent analysis thus provides valuable insights for understanding flow unsteadiness and informs flow control strategies. It helps predict effective actuation frequencies and highlights the corresponding forcing and response structures ideal for localized actuation (Yeh & Taira 2019; Ribeiro & Taira 2024). The strength of resolvent analysis also lies in its ability to capture non-normal effects, which appear when the eigenmodes of the linear operator are non-orthogonal. Non-normality can cause transient disturbance growth, even in flows that are linearly stable. By focusing on the most amplified dynamics driven by non-normal interactions, resolvent analysis exposes mechanisms that might not be detected through conventional stability analysis alone.

Resolvent analysis has been used for various flow problems, such as boundary layers (Dawson & McKeon 2020; Nogueira et al. 2020), turbulent channel flows (Moarref et al. 2013; Nakashima, Fukagata & Luhar 2017; Zhu, Chen & Fu 2024), jets (Schmidt et al. 2018; Pickering et al. 2021b) and airfoil wakes (Thomareis & Papadakis 2018; Symon, Sipp & McKeon 2019; Yeh & Taira 2019; Yeh et al. 2020). Among the latter, Yeh & Taira (2019) investigated the flow over a two-dimensional NACA0012 airfoil at a chord-based Reynolds number  $Re = 23\,000$  and two different angles of attack ( $\alpha = 6^{\circ}$  and  $9^{\circ}$ ), revealing a shear-layer dominated mechanism for energy amplification. Moreover, they used the findings from resolvent analysis to explore the capability of a thermal actuator, which introduces time-periodic heat injection, in suppressing stall and enhancing aerodynamic performance.

A higher Reynolds number ( $Re = 500\,000$ ) flow around a two-dimensional NACA0012 airfoil has also been investigated by Yeh *et al.* (2020). In this study, a windowed resolvent analysis was used to localize the forcing and response modes in the laminar separation bubble forming on the suction side of the airfoil. Windowed resolvent analysis has also been applied to identify amplification mechanisms driving the two-dimensional transonic buffet at Re = 2000 (Kojima *et al.* 2020). Resolvent-based control strategies have also been employed for three-dimensional separated flows (Ribeiro & Taira 2024), where the use of the optimal forcing modes has shown a reduction in the size of the separation region and the attenuation of the wing tip vortex.

Recently, there have been extensions to the original resolvent analysis to enable the use of unstable base flows. The incorporation of the eddy viscosity term in the resolvent analysis (Pickering *et al.* 2021*a*; Symon *et al.* 2023; von Saldern *et al.* 2024) models the nonlinear transfer of energy from large scales to small scales. The introduction of the eddy viscosity acts as a dampening and has shown leading modal structures to be in good agreement with modal structures uncovered from spectral proper orthogonal decomposition. Alternatively, discounted resolvent analysis (Jovanovic 2004; Jovanović & Bamieh 2005; Rolandi *et al.* 2024) allows examinations of the dynamics over a finite-time horizon, rather than the asymptotic behaviour. The latter approach, which is the one adopted in the present study, enables us to study unstable base flows. Both approaches modify the linear operator by shifting the eigenvalues in the stable part of the complex plane: the eddy resolvent does so by adding a dissipative term that mimics turbulent diffusion, while the discounted resolvent temporally windows the dynamics.

In this work, we use discounted resolvent analysis to investigate the effects of Reynolds numbers Re = 1000, 2500, 5000 and 10000 on separated flow over a NACA0012 airfoil. While previous investigations on separated flows around airfoils using biglobal linear analysis have predominantly focused on lower Reynolds numbers (He et al. 2017; Ribeiro et al. 2022; Tamilselvam, Asztalos & Dawson 2022; Nastro et al. 2023), or lower angles of attack when increasing the Reynolds number (Gupta et al. 2023), our work aims to address the transitional regime. Specifically, we analyse the linear amplification mechanisms over a range of Reynolds numbers, in a regime where the flow around the airfoil loses its periodicity and becomes highly unsteady. This change is associated with the transition from an oscillator-type behaviour, characterized by self-sustained, coherent unsteadiness, to an amplifier-type regime, where external perturbations are convected and selectively amplified by shear-layer instabilities. Our analysis centres on identifying dominant flow structures and characterizing their spatial and temporal behaviour, with particular attention to how these features evolve with increasing Reynolds numbers. Finding similarities and physics-based scalings is particularly beneficial in the moderate Reynolds number regime, with the potential to uncover underlying physics also present at higher Reynolds numbers commonly encountered in engineering applications.

The effects of Reynolds numbers are examined in relation to key parameters such as the temporal frequency, the spanwise wavenumber and the discount parameter, as summarized in figure 1, providing a comprehensive understanding of flow dynamics. Investigating the effect of spanwise wavenumber on the dominant flow structures reveals insights into the formation of three-dimensional structures, while analysing the effects of the discount parameter helps determine whether the dynamics evolve over different temporal scales. After introducing the theoretical background and numerical approach in § 2, § 3 examines how the Reynolds number affects the separated flow over the airfoil. Section 4 presents the resolvent mode structures and energy amplifications in relation to frequency, spanwise wavenumber and time scales. Finally, § 5 investigates the impact of a different angle of attack and discusses the scaling behaviour of dominant amplification mechanisms with respect to their characteristic frequencies.

#### 2. Theoretical background and numerical implementation

We analyse the spanwise periodic flow around a NACA0012 airfoil across various Reynolds numbers. Below, we present the biglobal resolvent analysis theoretical framework and outline the computational set-up employed in this study.

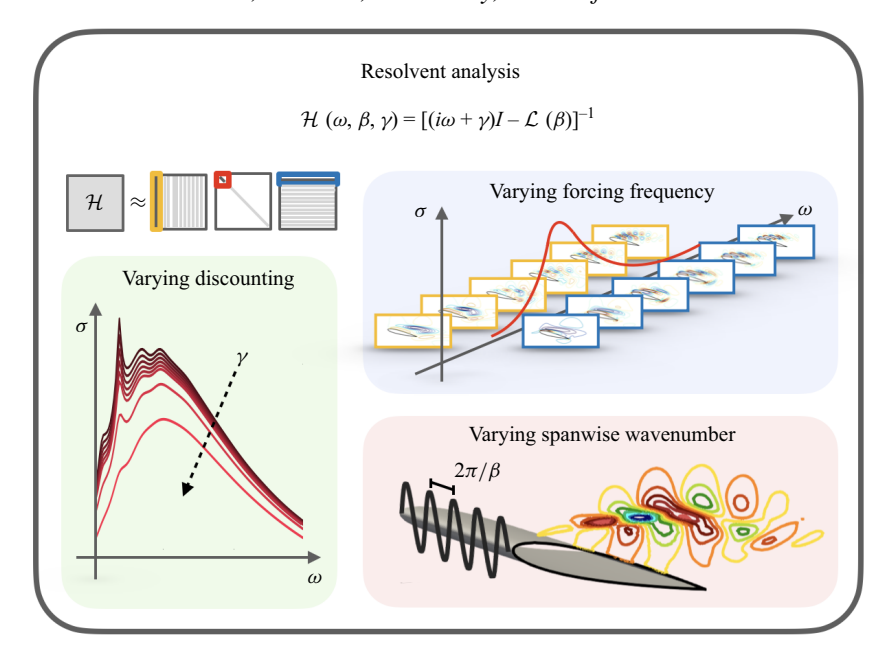


Figure 1. Overview of the present resolvent analysis.

# 2.1. Biglobal resolvent analysis

We consider the spatially discretized nonlinear governing equation,

$$\frac{\mathrm{d}\boldsymbol{q}}{\mathrm{d}t} = \mathcal{N}(\boldsymbol{q}),\tag{2.1}$$

where  $q = (\rho, \rho u, \rho e) \in \mathbb{R}^n$  represents the state vector,  $\rho$  is the density,  $u = (u_x, u_y, u_z)$  is the velocity vector with components along the streamwise (x), cross-stream (y) and spanwise (z) directions, and e is the energy. Here,  $\mathcal{N} \in \mathbb{R}^{n \times n}$  is the nonlinear Navier–Stokes evolution operator, and  $n = N \times 5$ , where N is the number of cells in the spatial discretization and the number of state variables is five. We now consider the flow field  $q = q_b + q'$  to be composed of the sum of a stationary base flow  $q_b$  and a fluctuating component q' of small amplitude. The base flow is considered to be the time- and spanwise-averaged flow. By substituting the decomposition in (2.1), and performing a Taylor expansion, we obtain the spatially discretized linearized governing equation for the fluctuating perturbation component, q':

$$\frac{\mathrm{d}q'}{\mathrm{d}t} = \mathcal{L}q' + f'. \tag{2.2}$$

Here,  $\mathcal{L} \equiv \nabla_{\boldsymbol{q}} \mathcal{N}|_{q_b} \in \mathbb{R}^{n \times n}$  is the linearized Navier–Stokes operator about the base flow,  $\boldsymbol{q}' \in \mathbb{R}^n$  is the perturbation and  $\boldsymbol{f}' \in \mathbb{R}^n$  collects the nonlinear terms (McKeon & Sharma 2010; Rolandi *et al.* 2024). Due to the temporal and spanwise homogeneity of the base flow, the response  $(\boldsymbol{q}')$  and forcing  $(\boldsymbol{f}')$  can be decomposed through a spatiotemporal Fourier transform as follows:

$$\mathbf{q}'(x, y, z, t) = \int_{-\infty}^{\infty} \int_{-\infty}^{\infty} \hat{\mathbf{q}}_{\omega, \beta}(x, y) e^{-i\omega t} e^{i\beta z} d\omega d\beta,$$

$$\mathbf{f}'(x, y, z, t) = \int_{-\infty}^{\infty} \int_{-\infty}^{\infty} \hat{\mathbf{f}}_{\omega, \beta}(x, y) e^{-i\omega t} e^{i\beta z} d\omega d\beta.$$
(2.3)

Here,  $\beta$  and  $\omega$  indicate the spanwise wavenumber and temporal frequency, respectively. By substituting these expressions into (2.2), we find the following input–output relationship:

$$\hat{\boldsymbol{q}}_{\omega,\beta}(\boldsymbol{x}) = (-i\omega\boldsymbol{I} - \mathcal{L}_{\beta})^{-1}\hat{\boldsymbol{f}}_{\omega,\beta}(\boldsymbol{x}) = \boldsymbol{H}_{\omega,\beta}\hat{\boldsymbol{f}}_{\omega,\beta}(\boldsymbol{x}), \tag{2.4}$$

where  $H_{\omega,\beta} \in \mathbb{C}^{n \times n}$  is the resolvent operator that acts as the transfer function between the forcing  $\hat{f}_{\omega,\beta}$  and the response  $\hat{q}_{\omega,\beta}$  at frequency  $\omega$  and spanwise wavenumber  $\beta$ .

Among all the possible forcing and response pairs that satisfy (2.4), resolvent analysis finds the optimal pair, i.e. those that maximize the energy at given values of  $\omega$  and  $\beta$ ,

$$\sigma^{2} = \max_{\hat{f}_{\omega,\beta}} \frac{\langle \hat{\boldsymbol{q}}_{\omega,\beta}, \hat{\boldsymbol{q}}_{\omega,\beta} \rangle_{E}}{\langle \hat{\boldsymbol{f}}_{\omega,\beta}, \hat{\boldsymbol{f}}_{\omega,\beta} \rangle_{E}} = \max_{\hat{\boldsymbol{f}}_{\omega,\beta}} \frac{||\hat{\boldsymbol{q}}_{\omega,\beta}||_{E}^{2}}{||\hat{\boldsymbol{f}}_{\omega,\beta}||_{E}^{2}}, \tag{2.5}$$

where  $||\cdot||_E$  is a suitable energy norm. In this work we consider the Chu norm (Chu 1965; George & Sujith 2011), which is expressed as

$$E_{Chu} = \frac{1}{2} \int_{V} \left( \bar{\rho} |\mathbf{u}|^{2} + \frac{a^{2} \rho^{2}}{\gamma \bar{\rho}} + \frac{\bar{\rho} c_{v} T^{2}}{\bar{T}} \right) dV, \tag{2.6}$$

where the variables with  $(\bar{\cdot})$  represent the base flow quantities. To take into account the energy norm, a similarity transform is applied to the resolvent operator. Therefore, we consider instead  $H_{\omega,\beta}^W = WH_{\omega,\beta}W^{-1}$ . Here, W is a volume-weighted matrix that allows us to express the energy norm in terms of the  $L_2$  norm for the singular value decomposition.

A singular value decomposition can now be performed on the weighted matrix. By retaining only the first  $m \ll n$  singular values and right/left singular vectors, we find a low-rank approximation of  $\boldsymbol{H}_{\omega,\beta}^W$ :

$$H_{\alpha\beta}^W \approx U \Sigma V^*.$$
 (2.7)

The columns of  $U = [u_1, u_2, \dots, u_m] \in \mathbb{C}^{n \times m}$  and  $V = [v_1, v_2, \dots, v_m] \in \mathbb{C}^{n \times m}$  hold the response and forcing modes, respectively, while  $\Sigma = \operatorname{diag}(\sigma_1, \sigma_2, \dots, \sigma_m) \in \mathbb{R}^m$  retains the gains of the corresponding forcing—response pairs.

In the present work, some cases are characterized by a linear dynamics that present eigenvalues with positive growth rate. For this reason, we use discounted resolvent analysis (Jovanovic 2004; Jovanović & Bamieh 2005), that considers a Laplace transform instead of a Fourier transform. This modification is equivalent to temporally damping the forcing and response by  $e^{-\gamma t}$ , which translates to considering the dynamic over finite time scales. A zero temporal damping  $\gamma = 0$ , when there are no unstable poles, corresponds to investigating the asymptotic (infinite-time) dynamics. Introducing  $\gamma \neq 0$ , we consider the dynamics over a finite-time horizon  $t_{\gamma} = 1/\gamma$ . To apply discounting, the integration line of the inverse Laplace transform is taken above all positive real parts of the eigenvalues of the linear operator. The discounted parameter  $\gamma$  is thus introduced, which must satisfy  $\gamma > \text{Re}\{\lambda\}$ , with  $\lambda$  being the eigenvalue of the linear operator with the largest real part. With discounting, the resolvent operator now reads

$$\mathbf{H}_{\omega,\beta} = [(\gamma - i\omega)\mathbf{I} - \mathcal{L}_{\beta}]^{-1}. \tag{2.8}$$

The singular value decomposition of the resolvent operator is approximated using the Krylov subspace projection method, with a subspace dimension for the reduced-order problem set to m = 24. Both the simulation of the base flow and resolvent analysis are performed within the compressible flow solver CharLES (Khalighi *et al.* 2011), coupled with the PETSc and SLEPc libraries (Roman *et al.* 2016; Balay *et al.* 2020) for the

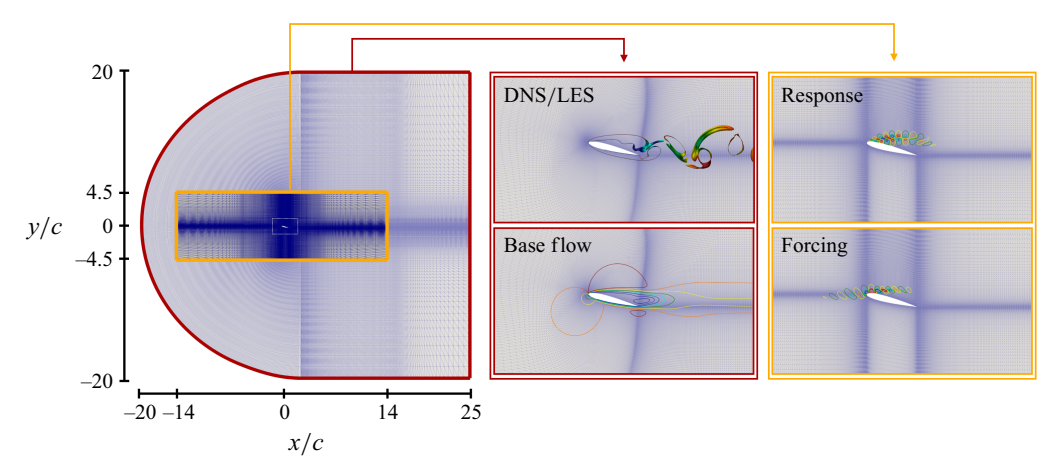


Figure 2. Computational set-up used for the base flow computation and resolvent analysis.

computation of the singular value decomposition. Further details on the formulation and implementation of resolvent analysis used herein can be found in Rolandi *et al.* (2024).

## 2.2. Computational set-up

We simulate the spanwise periodic flow around a two-dimensional NACA0012 airfoil at angles of attack 14° and 9° for a Reynolds number of  $Re = U_{\infty}c/v = 1000$ , 2500, 5000 and 10 000 and a Mach number of  $M_{\infty} = 0.1$ . Here,  $U_{\infty}$  indicates the free stream velocity, c the chord of the airfoil and v the kinematic viscosity. At these Reynolds numbers, the flow is three-dimensional, so a spanwise domain length  $L_z$  of one chord is considered for the computational domain. This choice is based on observations indicating that the flow transitions to a three-dimensional state with a spanwise wavelength of approximately  $\lambda_z \approx c/3$  (Gupta et al. 2023). The base flows are simulated with direct numerical simulations (DNS) for Re = 1000 and 2500 and wall-resolved large eddy simulations (LES) for Re = 5000 and 10 000. For the wall-resolved large eddy simulation, we use the Vreman subgrid-scale model (Vreman 2004). The boundary conditions are comprised of a no-slip adiabatic condition on the airfoil surface, uniform constant velocity, pressure, and temperature at the inlet and on far-field boundaries, a zero-pressure gradient at the outlet and periodic boundary conditions on the lateral sides. For each case, the time step is selected such that the local Courant–Friedrichs–Lewy number is less than unity.

The base flow is computed by time- and spanwise-averaging the instantaneous flow field over  $\sim 100$  convective times ( $t_c = tU_{\infty}/c$ ) after the transient is flushed out. Convergence of the base flow is checked by ensuring that the relative variation on the velocity flow field over the last five convective times satisfies

$$\frac{||\bar{\boldsymbol{u}}(t_{end}) - \bar{\boldsymbol{u}}(t_{end} - 5t_c)||_2}{||\bar{\boldsymbol{u}}(t_{end})||_2} < 0.01,$$
(2.9)

where  $\bar{u}$  is the time- and spanwise-averaged velocity flow field.

Details of the mesh used in this study are shown in figure 2. The red-framed domain indicates the computational domain used for computing the base flow and is extended to  $x/c \in [-20, 25]$ ,  $y/c \in [-20, 20]$  and  $z/c \in [0, 1]$ . The origin is positioned at the leading edge of the airfoil. For the biglobal resolvent analysis, the time- and spanwise-averaged base flow is interpolated onto a smaller two-dimensional grid, the yellow-framed grid, whose extent is  $(x/c, y/c) \in [-14, 14] \times [-4.5, 4.5]$ . This reduction is possible

	Case 1	Case 2	Case 3
Cells <sub>BF</sub> $N_{xy}$	$3.8 \times 10^{5}$	$6.5 \times 10^{5}$	$9.9 \times 10^{5}$
$Cells_{BF} N_z$	80	40	52
$L_z$	1.0	0.4	0.4
$egin{array}{c} L_z \ ar{\mathcal{C}}_D \ ar{\mathcal{C}}_L \end{array}$	0.2277	0.2180	0.2197
$ar{C}_L$	0.6879	0.6430	0.6474
Cells <sub>R</sub> $N_{xy}$	$1.3 \times 10^{5}$	$1.3 \times 10^{5}$	$2.3 \times 10^{5}$
$St^* = \arg\max\sigma_1$	2.81	2.72	2.83
St			

Table 1. Mesh convergence check for the  $Re = 10\,000$  case. Values of time-averaged drag  $(\bar{C}_D)$  and lift  $(\bar{C}_L)$  coefficients from the unsteady simulation together with frequency of maximum amplification from resolvent analysis at  $\beta = 0$  and  $\gamma = 1.25$  for the different meshes tested.

because the domain and grid resolution requirements for computing resolvent modes differ significantly from those used in unsteady simulations (Rolandi *et al.* 2024). Specifically, the modal structures are concentrated near the airfoil, eliminating the necessity for an extended domain, which is instead essential for the base flow simulations. Additionally, the grid refinement near the airfoil focuses on both the downstream and upstream regions, as the forcing modes develop upstream due to the convective nature of the amplification mechanisms.

We performed a grid convergence study using three meshes for the unsteady simulation to compute the base flow. In addition to these meshes, two meshes were tested for the resolvent analysis. In table 1, we report the results of the grid convergence study performed on the highest Reynolds number, Re = 10000. The combinations of the meshes used for the base flow computation and resolvent analysis are summarized in Case 1, Case 2 and Case 3. Cells<sub>BF</sub> and Cells<sub>R</sub> refer to the number of cells of the base flow mesh and resolvent analysis mesh, respectively. Number of cells on the xy-plane  $(N_{xy})$  and along the z-direction  $(N_z)$  are reported. The computational domain of Case 2 and Case 3 for the unsteady simulation of this Reynolds number extends over  $x/c \in [-20, 25], y/c \in$ [-20, 20] and  $z/c \in [0, 0.4]$ , given that the spanwise structures are smaller compared with the lower Reynolds number cases. The values of mean drag and lift coefficients from the unsteady simulation are shown, together with the frequency  $St^*$  of maximum gain from the resolvent analysis. Resolvent analysis for the grid study was performed considering  $\beta = 0$ and  $\gamma = 1.25$ . Overall, we can see convergence in the mean drag and lift coefficients and a relative difference between the results of  $St^*$  within 5 %. In figure 3, we present the 0-contour of the streamwise velocity for the time- and spanwise-averaged base flow for the three different cases. Additionally, we display the streamwise velocity contours of the response mode at  $\omega/2\pi = 2.7$ . The results of both the base flow and resolvent analysis with the different meshes are in good agreement. The meshes of Case 2 for both the unsteady simulation and resolvent analysis were used in this work.

In table 2, we provide details on the computational set-up in terms of number of grid points on the xy-plane  $N_{xy}$ , the number of grid points along the suction side of the airfoil section  $N_{airfoil}$  (symmetric with respect to the pressure side), the number of grid points in the spanwise direction  $N_z$  and its spanwise extent  $L_z$ , initial cell spacing on the wake  $\Delta x$  and vertical off-wall spacing  $\Delta y$ . The discretization details are reported for the unsteady simulation at the different Reynolds numbers, and for the mesh used for the resolvent analysis.

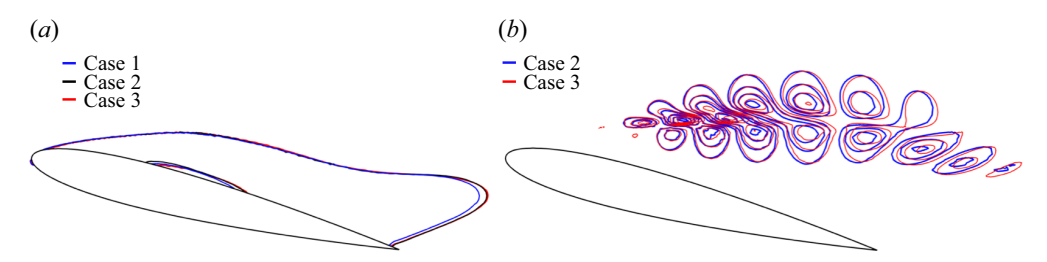


Figure 3. Mesh convergence check for the  $Re = 10\,000$  case. (a) Contour of time- and spanwise-averaged streamwise velocity  $\bar{u}_x = 0$ . (b) Contours of the streamwise velocity of the first response mode at frequency  $\omega/2\pi = 2.7$ ,  $\beta = 0$  and  $\gamma = 1.25$ .

Re	$N_{xy}$	$N_{airfoil}$	$N_z$	$L_z$	$\Delta x/c$	$\Delta y/c$
1000	$2.1 \times 10^{5}$	100	40	1	0.005	0.005
2500	$3.8 \times 10^{5}$	160	50	1	0.001	0.001
5000	$3.8 \times 10^{5}$	160	50	1	0.001	0.001
10 000	$6.5 \times 10^{5}$	200	40	0.4	0.001	0.0005
Resolvent	$1.3 \times 10^{5}$	100	1	_	0.005	0.003

Table 2. Mesh details for the unsteady simulation of the different Reynolds numbers and resolvent analysis.

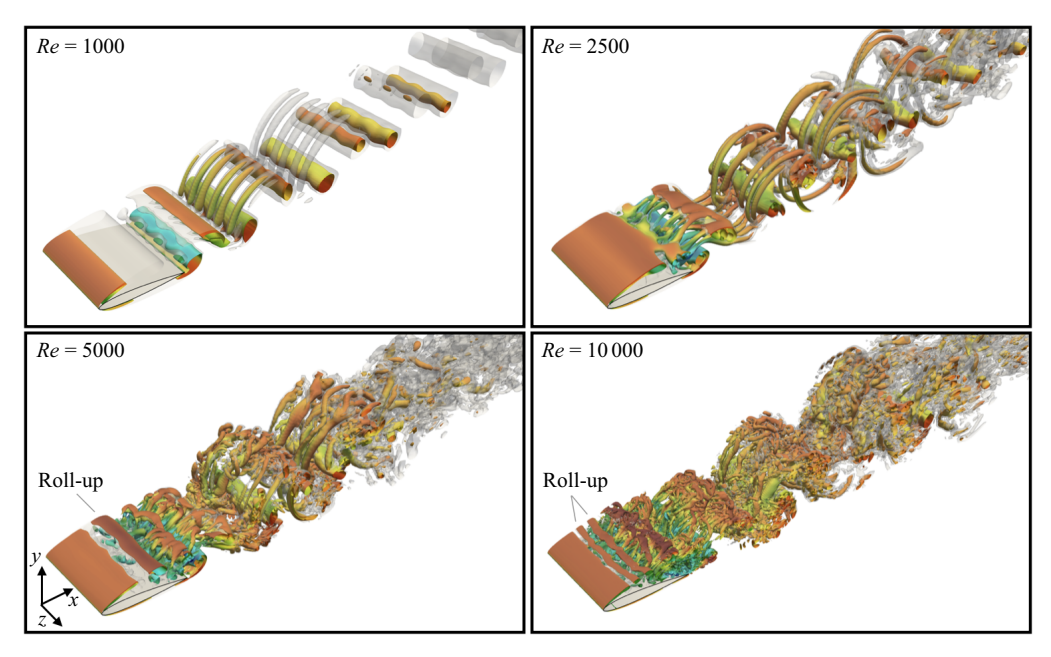


Figure 4. Instantaneous flow fields around a NACA0012 airfoil at  $\alpha=14^{\circ}$  and different Reynolds numbers. Visualization of isosurfaces of Q-criterion Q=0.05, coloured by streamwise velocity, and Q=0.005 in translucent.

## 3. Reynolds number effects on the unsteady and base flows

## 3.1. Unsteady flows

The flow fields around a NACA0012 airfoil at an angle of attack of  $14^{\circ}$  for the considered Reynolds numbers are shown in figure 4(a-d). At these Reynolds numbers, the flow is

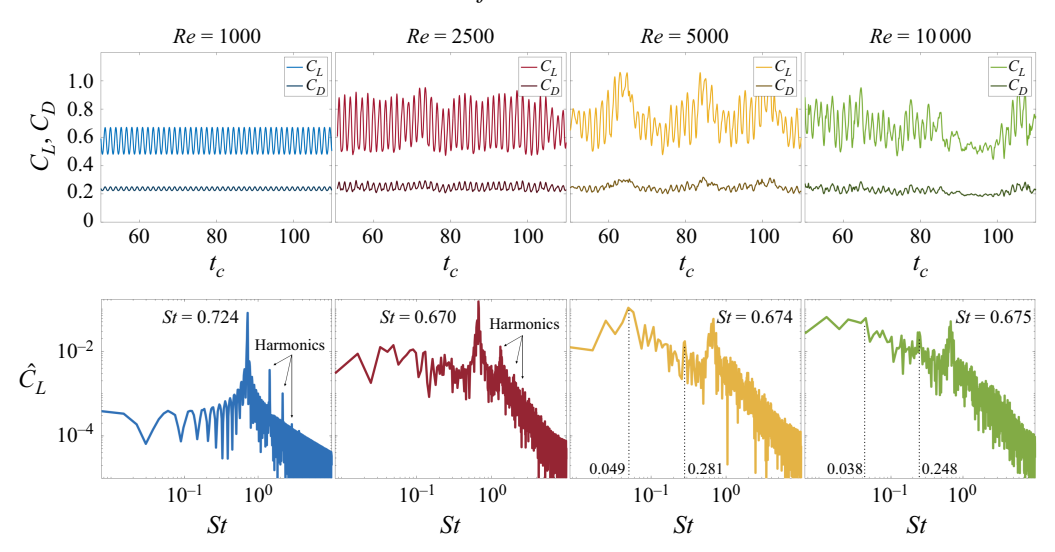


Figure 5. Lift coefficient  $C_L$ , drag coefficient  $C_D$  and lift spectra  $\hat{C}_L$  at the different Reynolds numbers.

unsteady and exhibits the characteristic von Kármán vortex shedding in the wake region. The flow around the airfoil at  $\alpha=14^{\circ}$  undergoes a transition from steady state to periodic at approximately  $Re\approx380$  through a Hopf bifurcation (Rolandi *et al.* 2022). As the Reynolds number increases further, the periodic flow transitions to three-dimensional dynamics through a period-doubling bifurcation, also known as the Mode C instability (Sheard *et al.* 2005*a*; Meneghini *et al.* 2011; Rolandi 2021). The Reynolds number at which the flow becomes three-dimensional at this angle of attack is between Re=750 and 1000 (Gupta *et al.* 2023). This transition is characterized by the emergence of a subharmonic component of the vortex shedding, effectively doubling the flow periodicity. Notably, period-doubling bifurcations are also associated with the onset of chaos in fluid flows (Pulliam & Vastano 1993), through the so-called period-doubling cascade.

The three-dimensional flow resulting from this transition features spanwise structures that develop across the airfoil. The Mode C instability develops in the stretched region between two consecutive vortices, called the braid region, and results in the formation of elongated streamwise vortices. At Re=1000, the spanwise wavelength of the three-dimensional structures is approximately  $\lambda_z \approx c/3$ , consistent with previous studies (Gupta et al. 2023), where the stability of the periodic solution was examined through Floquet analysis. As the Reynolds number increases further, the shear layer separating from the leading edge becomes unstable. The shear layer rolls up closer to the leading edge, forming two-dimensional spanwise vortical structures, that are related to the Kelvin–Helmholtz instability. The characteristic length of the vortical spanwise elongated structures decreases with the Reynolds numbers (see figure 4c-d). Finally, these structures are convected downstream, where they break down into smaller, three-dimensional structures, contributing to the increasing level of turbulence in the flow.

We report the time evolution of the drag and lift coefficients in figure 5, together with the frequency spectra of the lift coefficients in terms of Strouhal number  $St = cf/U_{\infty}$ , where f indicates the frequency. For the case of Re = 1000, we observe a clear peak at St = 0.72 and its harmonics, due to the periodicity of the flow at this Reynolds number. A clear peak and its harmonics are also visible at Re = 2500, with the low-frequency contents becoming increasingly energetic. At this Reynolds number, the oscillations have higher amplitude compared with Re = 1000 and the peak is at a lower frequency corresponding

to St=0.67. Increasing the Reynolds number further, the frequency peak of the wake oscillation for both Re=5000 and  $10\,000$  occurs at  $St\approx0.67$ , as for the Re=2500 case. However, the amplitudes of the spectral peak reduce with the Reynolds number, consistent with the decreasing oscillatory type behaviour. At these Reynolds numbers, we also observe a broader frequency spectrum and the emergence of slower dynamics, visible in the  $C_L$  and  $C_D$  variations, which are associated with the interaction between the separated shear-layer roll-up and the airfoil (Zaman, McKinzie & Rumsey 1989; Mukai, Enomoto & Aoyama 2006). For Re=5000, these slower dynamics occur at  $St\approx0.05$  and  $St\approx0.28$ , while for  $Re=10\,000$ , they appear at  $St\approx0.04$  and  $St\approx0.24$ .

To further investigate the slower dynamics observed in the lift spectra at Re = 5000 and  $10\,000$ , we focus on the Re = 5000 case. Figure 6 presents the frequency-filtered time evolution of the lift coefficient for the Re = 5000 case. Specifically, we examine the low-frequency range 0 < St < 0.1 and the midfrequency range 0.2 < St < 0.4, targeting the spectral peaks at  $St \approx 0.05$  and  $St \approx 0.28$ , respectively, as reported in the lift spectra in figure 5 for the Re = 5000 case. Instantaneous spanwise vorticity fields corresponding to the crests and troughs of the filtered signals are also shown. The vorticity fields at the troughs of the low-frequency signal, at  $t = t_L^1$ ,  $t_L^3$  and  $t_L^5$  in figure 6(a), have similar flow characteristics. The separated shear layer is elongated and rolls up farther downstream from the leading edge, with vortex cores forming at streamwise locations x > 0.7. This positioning keeps the vorticity detached from the airfoil's suction surface, thereby limiting the development of induced vorticity of opposite-sign near the surface. As a result, the flow is massively separated from the airfoil.

In contrast, at the crests of the low-frequency signal, at  $t=t_L^2$ ,  $t_L^4$  and  $t_L^6$ , the shear layer rolls up much closer to the suction surface x<0.7, leading to the generation of strong opposite-sign vorticity. This causes the flow to locally form a secondary recirculation region with higher and positive streamwise velocity on the airfoil surface, generating local low-pressure zones, which enhance the lift force. This suggest that the low-frequency behaviour is associated with the formation of the secondary recirculation region (Zaman *et al.* 1989; Broeren & Bragg 1998; Mukai *et al.* 2006). Therefore, the flow alternates between two states: (i) a massive separated flow with a negligible secondary recirculation region ( $t=t_L^1$ ,  $t_L^3$  and  $t_L^5$ ) and (ii) a separated flow coexisting with a secondary recirculation region ( $t=t_L^2$ ,  $t_L^4$  and  $t_L^6$ ). The two states depend on the roll-up location of the separated shear layer. We also note that the low frequency dynamics ( $St \approx 0.05$ ) are an order of magnitude lower than the vortex shedding ( $St \approx 0.67$ ), which is in agreement with previous studies (Zaman *et al.* 1989; Broeren & Bragg 1998), which associate this mechanism with the breathing of the laminar separation bubble.

We now consider the midfrequency signal, bandpass-filtered over 0.2 < St < 0.4. In figure 6(b), we observe that at the crests of the signal, at  $t = t_M^1$ ,  $t_M^3$  and  $t_M^5$ , the shear-layer vortex has not fully rolled-up. On the contrary, at the through of the signal,  $t_M^2$ ,  $t_M^4$  and  $t_M^6$ , the leading-edge vortex is rolled-up, forming a defined single vortical structure detached from the downstream same sign negative vorticity. Some works link these dynamics to vortex pairing (Tang *et al.* 2021).

The lift coefficient signal effectively captures the dynamics of large vortex shedding in the wake, and the slow dynamics of the separation region. However, our interest also lies in the dynamics of the separated shear layer, which manifests as the leading-edge vortex rollup. To investigate the shear-layer dynamics, we compute the energy spectra from the shear layer at various streamwise positions: x/c = 0.25, 0.5, 0.75 and 1, along 0 < y/c < 0.25, as shown in figure 7.

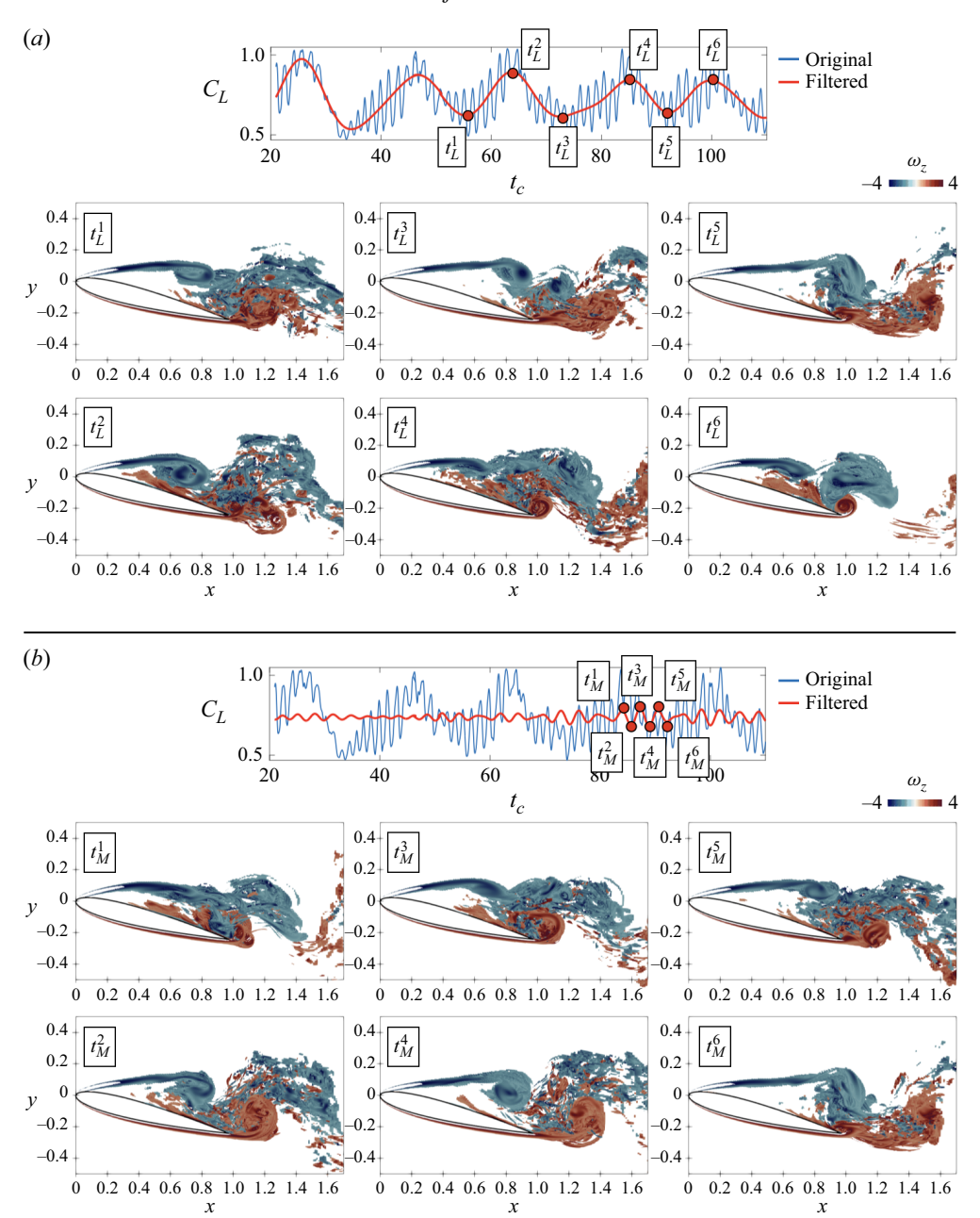


Figure 6. Instantaneous lift coefficient at Re = 5000: (a) low-pass-filtered over St < 0.1; (b) bandpass-filtered over 0.2 < St < 0.4. Instantaneous spanwise vorticity fields are shown at instants indicated by the red dots.

At Re = 1000, the flow is periodic, with the energy spectra at each position showing a dominant peak corresponding to vortex shedding. At x/c = 1, the subharmonic becomes significant, indicating a period-doubling instability of the NACA0012 periodic shedding that leads the transition to three-dimensional flow (Sheard *et al.* 2005*b*; Meneghini *et al.* 2011; Rolandi 2021; Gupta *et al.* 2023). At Re = 2500, the harmonic components become more prominent, and at even higher Reynolds numbers, the spectrum broadens

## L.V. Rolandi, L. Smith, M. Amitay, V. Theofilis and K. Taira

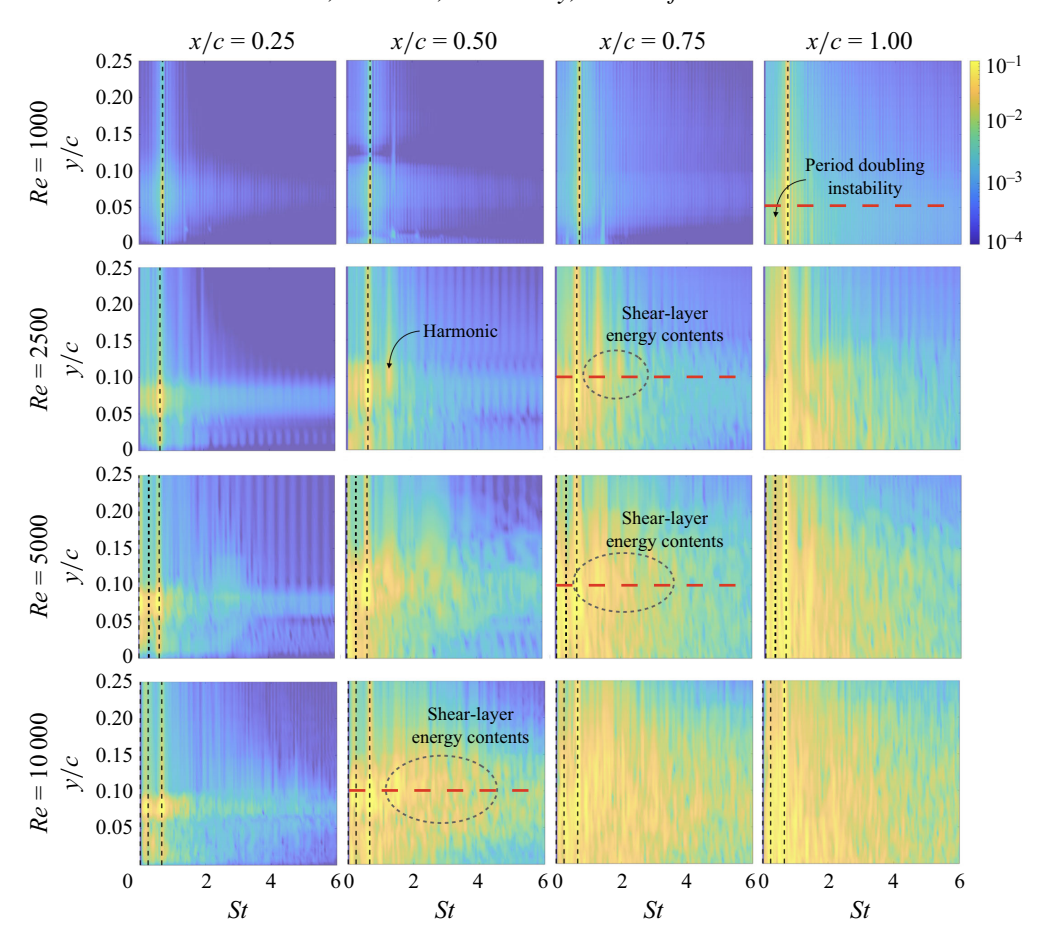


Figure 7. Contours of energy spectra at Re = 1000, 2500, 5000 and 10 000. Contours are shown at different streamwise locations x/c along  $y/c \in [0, 0.25]$ . Black dashed lines indicate the dominant frequency peaks associated with the lift coefficient, see figure 5. Red horizontal lines indicate the vertical locations considered in figure 8.

significantly, especially as the streamwise position approaches the wake. Also for the higher Reynolds number cases, we observe the presence of subharmonics, which, in this case, correspond to vortex pairing within the shear layer. For  $Re \geqslant 2500$ , the highest energy amplitudes at x/c = 0.25 and 0.5 are concentrated at a specific cross-stream location, approximately  $y/c \approx 0.1$ . This identifies a broad region of high-frequency, high-amplitude unsteadiness associated with the shear-layer dynamics at the subsequent streamwise positions.

For the specific locations indicated by the red dashed lines in figure 7, we also present the spectra of the vertical velocity in figure 8. As the Reynolds number increases, we observe a gradual intensification of the harmonic peaks, reflecting enhanced nonlinear interactions (Deissler 1969). This is particularly evident at Re = 2500, where higher-order harmonics becomes clearly distinguishable, and at Re = 5000 where the first harmonic is highly energetic. At the highest Reynolds number, Re = 10000, the spectrum becomes noticeably broader. The dominant energy shifts towards higher frequencies, with the maximum peak occurring at  $St \approx 2.6$ , which indicates the shear-layer roll-up, as will be discussed later.

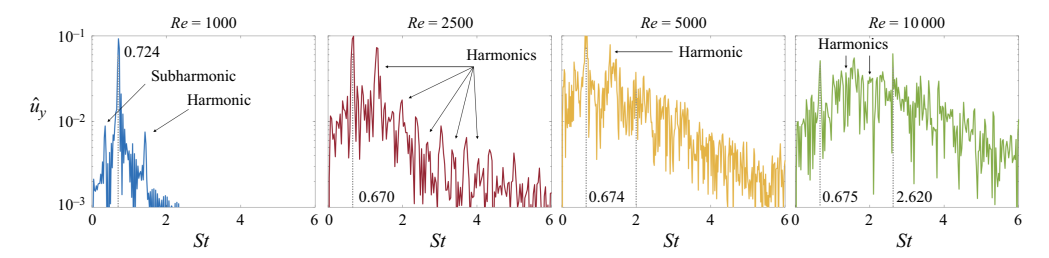


Figure 8. Vertical velocity spectra  $\hat{u}_y$  at locations indicated by the the red dashed lines in figure 7 at the different Reynolds numbers.

## 3.2. Oscillator and amplifier dynamics

The spectral change observed in figures 7 and 8 reflects the transition between oscillator-to amplifier-type behaviour (Towne *et al.* 2015; Rosenberg, Symon & McKeon 2019; Symon *et al.* 2019). Oscillator flows exhibit intrinsic global instabilities that give rise to self-sustained unsteadiness. In contrast, amplifiers are convectively unstable and amplify external disturbances.

At low Reynolds number, Re < 2500, the flow exhibits narrow-band spectral peaks with clear harmonics, characteristic of an oscillator-type dynamics. As the Reynolds number increases, Re > 2500, the frequency spectrum broadens significantly and energy shifts towards higher frequencies. This broadening reflects the transition to an amplifier-type regime dominated by shear-layer instabilities.

## 3.3. Time-averaged base flows

The unsteady flow field is averaged in time and along the spanwise direction to obtain the base flow for the resolvent analysis. The resulting streamwise velocity fields are shown in figure 9 for the considered Reynolds numbers. As the Reynolds number increases, the shear layer separating from the leading edge becomes progressively thinner and curves due to stronger reverse flow in the recirculation region.

The corresponding zero streamwise velocity contours of the time- and span-averaged base flows are visualized in figure 9(e). At Re = 1000, the base flow features a single recirculation region, which is elongated compared with those at higher Reynolds numbers. When the Reynolds number is increased to Re = 2500, the recirculation region shortens before being stretched again at higher Reynolds numbers. For  $Re \ge 2500$ , the base flow exhibits a secondary recirculation region on the airfoil's suction side, which shifts upstream and becomes thinner as the Reynolds number increases.

The secondary recirculation region is caused by the induced vorticity generated in the separated region on the suction side, as previously discussed. Additionally, the separation point of the primary recirculation region shifts upstream with increasing Reynolds number (Counsil & Goni Boulama 2013; Brunner *et al.* 2021). This behaviour is due to a higher adverse pressure gradient near the leading edge of the airfoil due to the thinning of the boundary layer over the airfoil upstream of the separation point with increasing Reynolds number.

#### 4. Resolvent analysis

In this section, we present the results of the resolvent analysis, organized into three parts. First, we examine the eigenvalues of the linear operators to establish an appropriate range for the discount parameter  $\gamma$ . Second, we investigate the influence of the spanwise

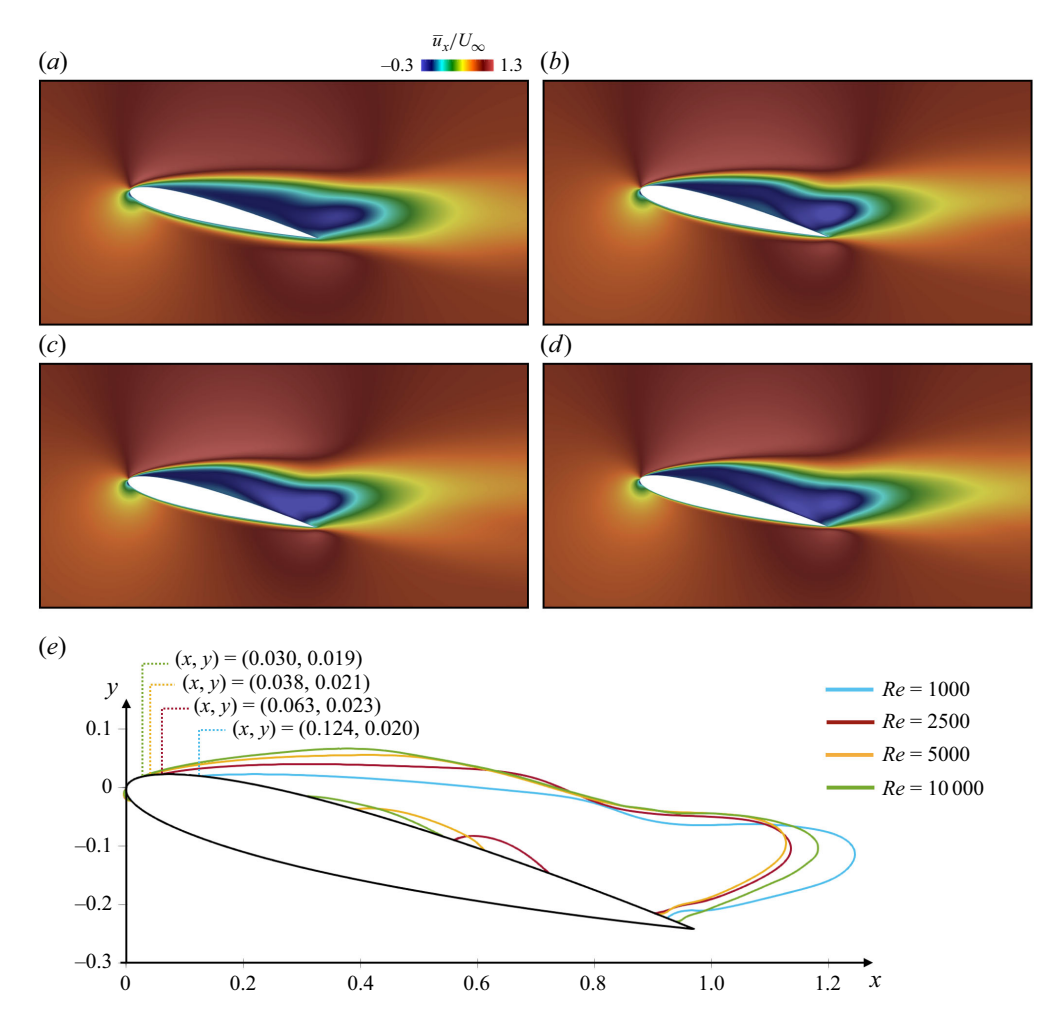


Figure 9. Time- and spanwise-averaged (base flow) streamwise velocity around a NACA0012 wing at  $\alpha = 14^{\circ}$  and (a) Re = 1000, (b) 2500, (c) 5000 and (d) 10 000. (e) Contour of time- and spanwise-averaged streamwise velocity  $\bar{u}_x = 0$ .

wavenumber  $\beta$  on the system. Last, we examine how modal structures and energy gain vary with the Reynolds number across a range of frequencies.

#### 4.1. Eigenvalue decomposition of the linear operator

Let us examine the eigenvalues of the linearized Navier–Stokes operator at the different Reynolds numbers by solving the eigenvalue problem

$$\mathcal{L}\boldsymbol{\phi} = -i\lambda\boldsymbol{\phi},\tag{4.1}$$

where  $-i\lambda = -i(\lambda_r + i\lambda_i)$  is the complex eigenvalue and  $\phi$  is the corresponding eigenvector. Here, we consider  $\mathcal{L} = \mathcal{L}_{\beta=0}$ , while the effect of spanwise wavenumber  $\beta \neq 0$  will be explored in § 4.3. This allows us to consider appropriate ranges for the discount parameter depending on whether we consider two-dimensional  $\beta = 0$  or three-dimensional  $\beta \neq 0$  perturbations.

In figure 10(a), the eigenvalue with the largest real part for each Re is shown in the complex plane. Both the growth rate and frequency increase with increasing

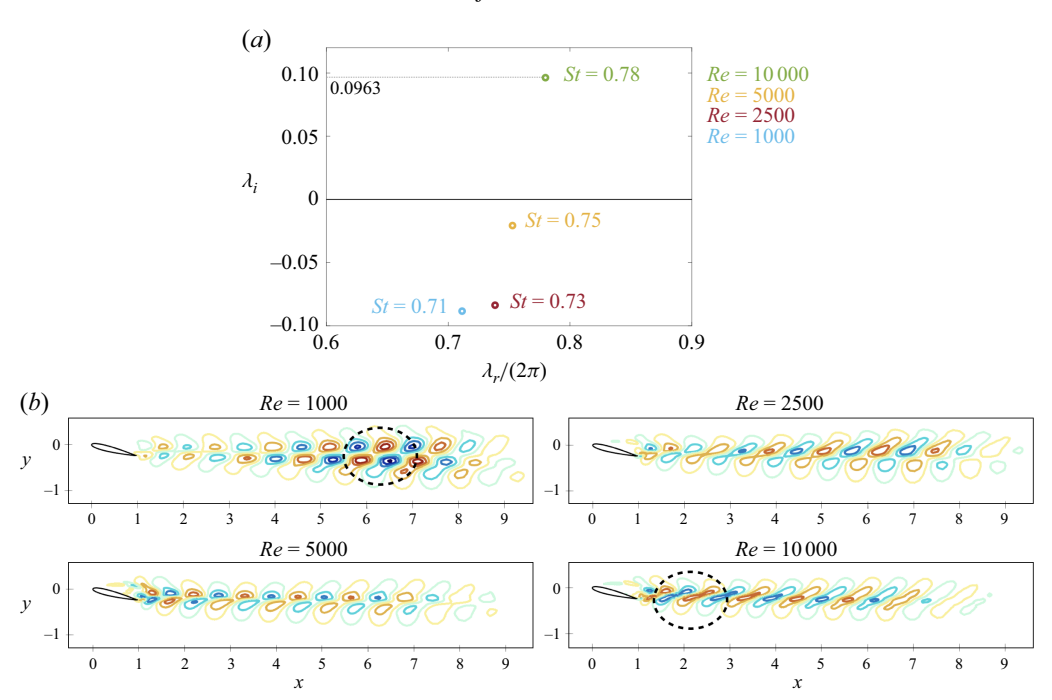


Figure 10. (a) The eigenvalues with the largest real component  $Re\{-i\lambda\} = \lambda_i$  and (b) corresponding eigenvectors shown by contours of real part streamwise velocity. Dashed circles mark the region of maximum modal structure amplitude.

Reynolds number. The linear dynamics has an eigenvalue with a positive real part  $Re\{-i\lambda\} = \lambda_i$  only at  $Re = 10\,000$ , with  $\lambda_i = 0.0963$ . For the lower Reynolds number cases, all the eigenvalues have negative real parts, despite the unsteady nature of the nonlinear dynamics. In this regard, it should be considered that the eigenvalue analysis depends on the choice of the base flow and that there are conditions for the validity of mean flow stability analysis (Beneddine *et al.* 2016).

In fact, it is important to consider that stability analysis based on the time-averaged flow (not an exact solution of the Navier–Stokes equations) needs to be performed with care. Moreover, it has been shown that flows exhibiting quasimonochromatic oscillations can yield different linear responses when analysed about the time-averaged flow versus the underlying unstable fixed point (Barkley 2006; Turton, Tuckerman & Barkley 2015; Rolandi 2021). The results of  $Re\{-i\lambda\} < 0$  even at Re = 1000 are somewhat counterintuitive, as oscillator-type flows are expected to exhibit a global instability at the vortex shedding frequency. However, for this type of flow, this expectation applies to stability analysis about the fixed point, not the time-averaged flow. In fact, previous studies have shown that the stability analysis about the fixed-point solution at Re = 1000 and  $\alpha = 14^{\circ}$  exhibits a positive growth rate (Rolandi *et al.* 2022). Nevertheless, we present here the eigenvalue analysis of the linear operator linearized around the time-averaged flow, as this constitutes a necessary step for the subsequent discounted resolvent analysis.

From the result shown in figure 10(a), we observe a monotonic increase of  $\lambda_i$  with respect to the Reynolds number, with a linear increase for  $Re \ge 2500$ . We can then infer that the eigenvalue based on the time-averaged base flow crosses the imaginary axis at  $Re \approx 5900$ . The corresponding eigenvectors are shown in figure 10(b). At Re = 1000 the modal structure is mainly concentrated in the wake region, while at higher

## L.V. Rolandi, L. Smith, M. Amitay, V. Theofilis and K. Taira

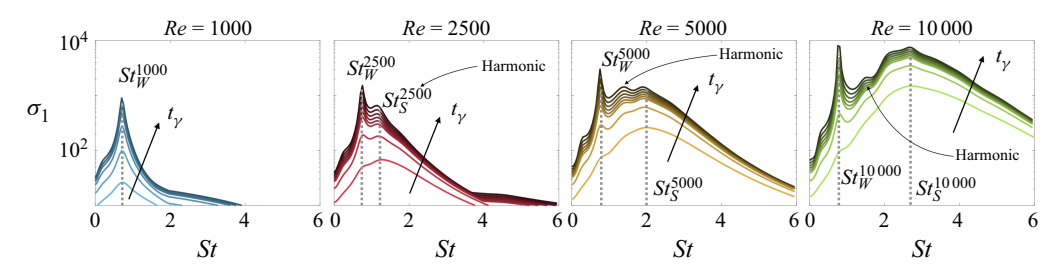


Figure 11. Variation of the first singular value  $\sigma_1$  with respect to frequency for different finite-time horizon  $t_{\gamma} \in [0.8; 6.67]$  at Re = 1000, 2500, 5000 and 10 000. Dashed grey lines indicate the frequencies of maximum gain at short and long time scales.

Reynolds numbers they also exhibit structures in the shear-layer region. As the Reynolds number increases, the position of maximum modal structure amplitude, indicated by the dashed circle, shifts from the far wake (at Re = 1000) to the near wake (at Re = 1000). Furthermore, for  $Re \ge 2500$ , the modal structure appears not only in the wake but also in the shear layer. This reflects the fact that for these Reynolds numbers the shear layer rolls up and interacts with the wake dynamic.

## 4.2. Temporal discounting

Once the eigenvalues are found, the discount parameter for the resolvent analysis is chosen such that  $\gamma > \max\{\text{Re}\{-i\lambda\}, 0\}$ . This allows us to consider the overall forced dynamics over a time scale shorter than the time scale associated with  $\text{Re}\{-i\lambda\}$ . Longer time scales should not be considered, because the implication of having a positive real part  $\text{Re}\{-i\lambda\} > 0$  would make the response seemingly unbounded as  $t \to \infty$ , masking the effect of forcing.

Here, a value of  $\gamma > 0.0963$  for  $Re = 10\,000$  corresponds to dynamics within a finite time horizon  $t_{\gamma} < 10.4$ . The effect of discounting on the energy amplification is shown in figure 11. The variations of the first singular value as a function of the frequency are plotted for  $\gamma = \{0.15, 0.20, 0.25, 0.30, 0.40, 0.625, 1.25\}$  corresponding to  $0.8 \le t_{\gamma} = 1/\gamma \le 6.67$ . The frequency is considered in terms of Strouhal number  $St = c\omega/(U_{\infty}2\pi)$ . Considering this range of  $t_{\gamma}$ , in what follows we will refer to  $t_{\gamma} = 0.8$  as the short time scale and  $t_{\gamma} = 6.67$  as the long time scale.

At Re = 1000, only one peak emerges as  $t_{\gamma}$  varies, while for  $Re \ge 2500$  two distinct peaks are observed, as indicated by the dashed lines in figure 11. The first peak appears at a high frequency on the short time scale, while on the long time scale, another peak at a lower frequency dominates. For all Reynolds numbers, the long time scale peak occurs at a frequency corresponding to the eigenvalue with the maximum real part. This is because, with lower  $\gamma$  (higher  $t_{\gamma}$ ), the inverse Laplace integration is closer to such an eigenvalue, and the norm of the resolvent operator increases at that frequency.

By comparing figure 11 with figure 8, we observe a clear correspondence between the gain peaks and the spectral content of the vertical velocity. In addition to the low-frequency peaks  $St_W$  associated with vortex shedding, the gain shifts towards higher frequencies as the Reynolds number increases. At Re = 2500, the second peak  $St_S^{2500}$  aligns with the first harmonic observed in figure 8, while at higher Reynolds numbers, the influence of higher-order harmonics remains evident in the gain distribution over longer time scales. Notably, at  $Re = 10\,000$ , the high-frequency peak in the gain  $St_S^{10\,000}$  matches the highest frequency observed in the vertical velocity spectra in figure 8.

In figure 12, we show the streamwise velocity components of the first response mode at short and long time scale and at the frequencies  $St_W$  and  $St_S$ , indicated in figure 11.

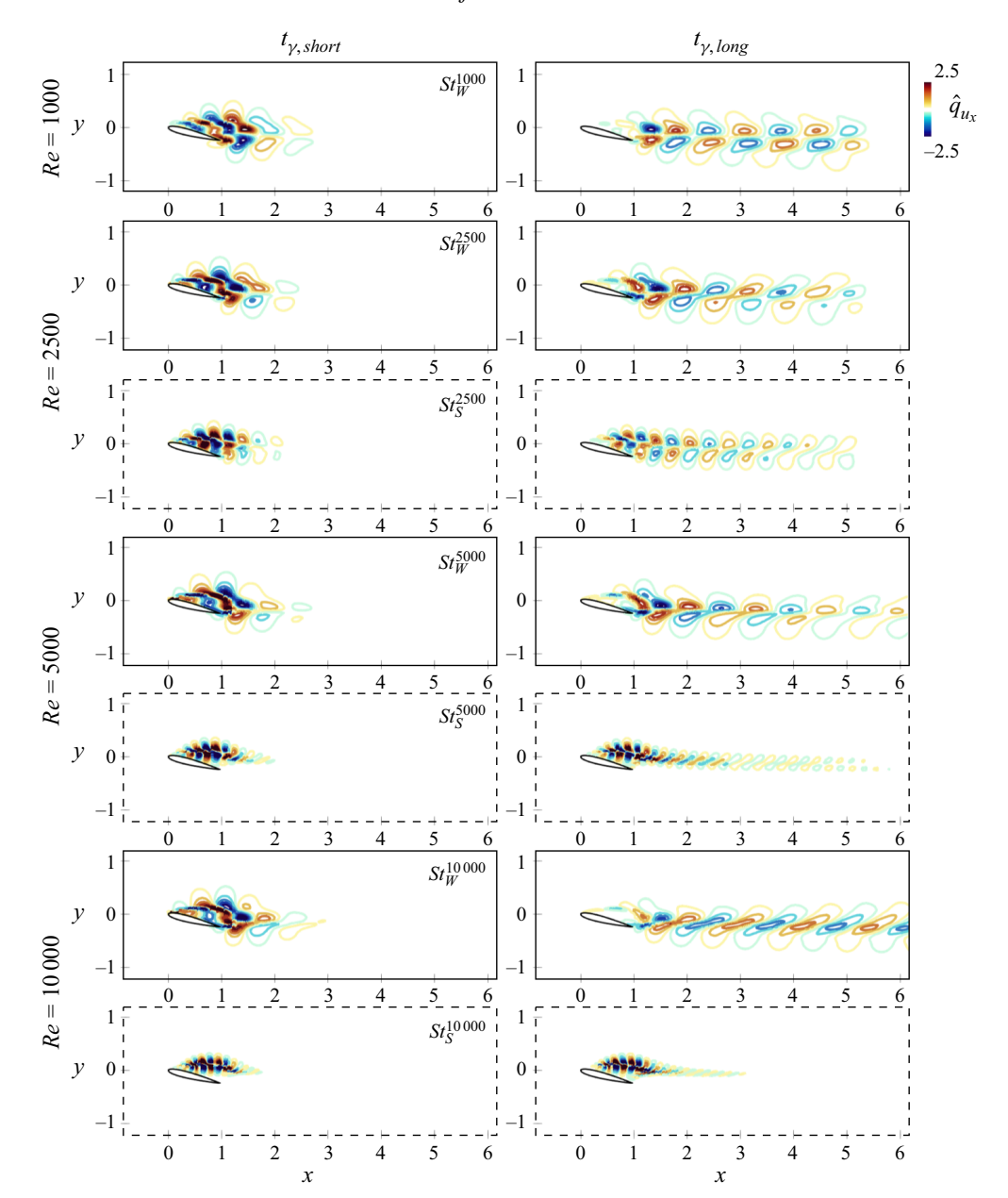


Figure 12. Contours of streamwise velocity component of the first response mode at the frequencies of maximum gain at short and long time scales. Here ( $\longrightarrow$ ) line frame indicates the mode at the lower frequency peak,  $St_W$ , and (- - - -) line frame indicates the mode at the higher frequency peak,  $St_S$ .

Frequencies  $St_W$  and  $St_S$  correspond to the short and long time scale peaks, respectively. At the lower frequencies,  $St_W$ , we observe that the structures emerge in the wake and highlight the coupling between the leading and trailing edge, we will therefore refer to this mode as the wake mode. We also note that the modal structures at the lowest Reynolds number are similar to the structures revealed from non-modal stability analysis of low-Reynolds number flow (He *et al.* 2017) when increasing the time horizon. On the other hand, at the higher frequency peak,  $St_S$ , the structures are present in the shear-layer region

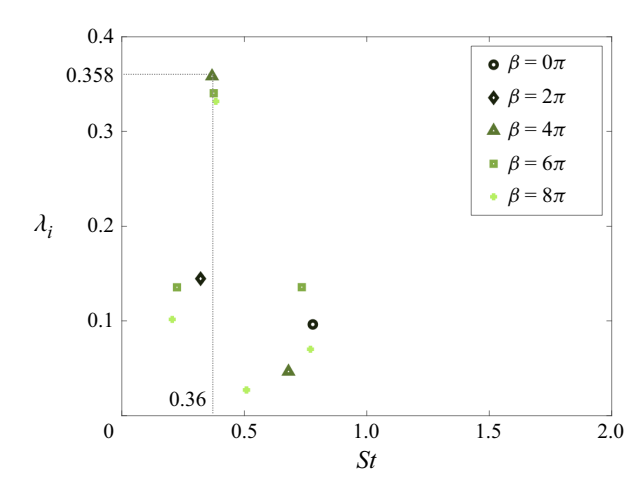


Figure 13. The eigenvalues with the largest real components for different  $\beta$  at  $Re = 10\,000$ .

detaching from the leading edge. We therefore refer to this mode as the shear-layer mode. For both the wake and shear-layer modes, we observe that the structures at  $t_{\gamma,short}$  are closer to the airfoil, while they develop downstream when increasing  $t_{\gamma}$ . This corresponds to the fact that the perturbation has more time to grow, and translates into the higher energy gain shown in figure 11. Further discussion on the effects of discounting can be found in Appendix A.

## 4.3. Spanwise wavenumber effects

In this subsection, we consider the effects of the spanwise wavenumber  $\beta$ . Firstly, we need to compute the eigenvalues of the linear operator  $\mathcal{L}_{\beta}$  at varying  $\beta$ , as we performed for the  $\beta=0$  case. In figure 13 the unstable eigenvalues are shown in the complex plane for  $\beta\in[0,8\pi]$ . The eigenvalue with the largest real part corresponds to  $\beta=4\pi$  at  $St=\lambda_r/(2\pi)=0.36$ , and the real part decreases at the same frequency for increasing wavenumber. In this case, the value of the largest real part  $\lambda_i=0.358$  suggests that we should consider dynamics within a time scale of  $t_\gamma\approx 2.8$ , shorter compared with the  $\beta=0$  investigated in the previous subsection. The effects of spanwise wavenumber  $\beta$  at short  $(t_\gamma=0.8)$  and medium  $(t_\gamma=2.5)$  time scales are shown in figures 14 and 15, respectively. The gain distributions for the first three singular values  $(\sigma_1, \sigma_2 \text{ and } \sigma_3)$  are shown over the  $\beta-St$  plane for the different Reynolds numbers. The peaks of the spectral content of the lift coefficient, shown in figure 5, are also reported for comparison.

For the short time scale,  $t_{\gamma}=0.8$ , we observe that the overall distributions of  $\sigma_1, \sigma_2$  and  $\sigma_3$  show some similarities across different Reynolds numbers. For  $\sigma_1$ , the maximum gain is achieved at  $\beta=0$ . The singular values  $\sigma_2$  and  $\sigma_3$  are instead more sensitive to the spanwise variation. In particular, the variation of  $\sigma_2$  and  $\sigma_3$  across  $\beta$  and St are similar, with maximum values achieved at low frequency and spanwise wavenumbers that increase with the Reynolds number. Overall, the second and third singular modes, even at short time scales, seem to reflect the development of smaller structures in the flow when increasing the Reynolds number, while the first singular value mostly reflects the two-dimensional dynamics.

The matter changes when we consider longer time scales, as shown in figure 15. Increasing  $t_{\gamma}$ , several mode switchings are observed. These appear at low frequencies, particularly close to the characteristic frequencies at the highest Reynolds numbers and evident from a change in the gain variation. This indicates that higher-order modes, which

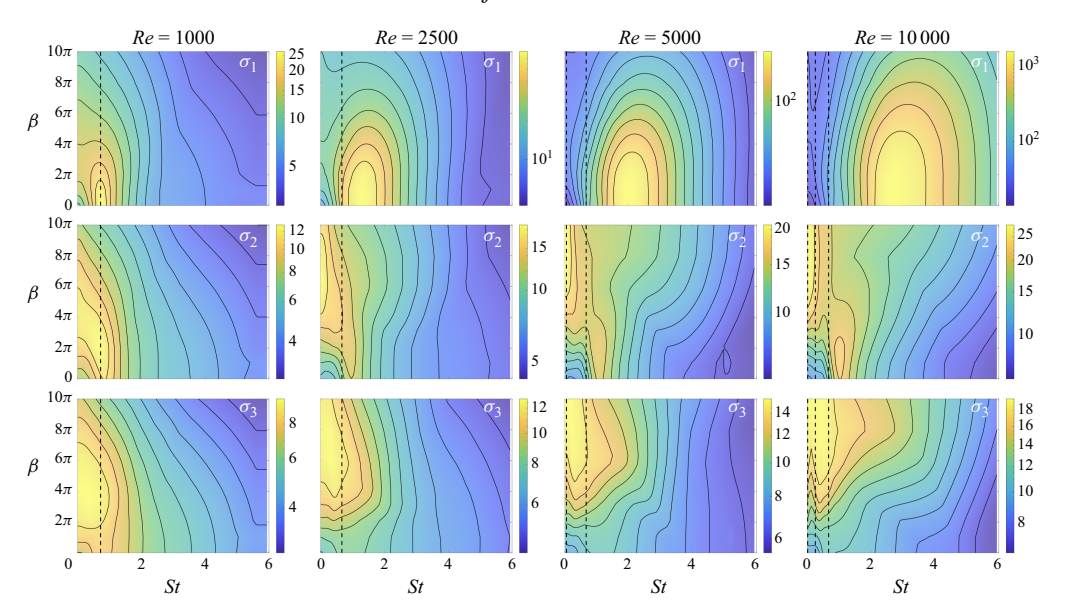


Figure 14. Gain distributions of the first three singular values over the  $\beta - St$  plane at Re = 1000, 2500, 5000 and 10 000 at  $t_{\gamma} = 0.8$ . Black dashed lines indicate the dominant frequency peaks associated with lift coefficients (see figure 5).

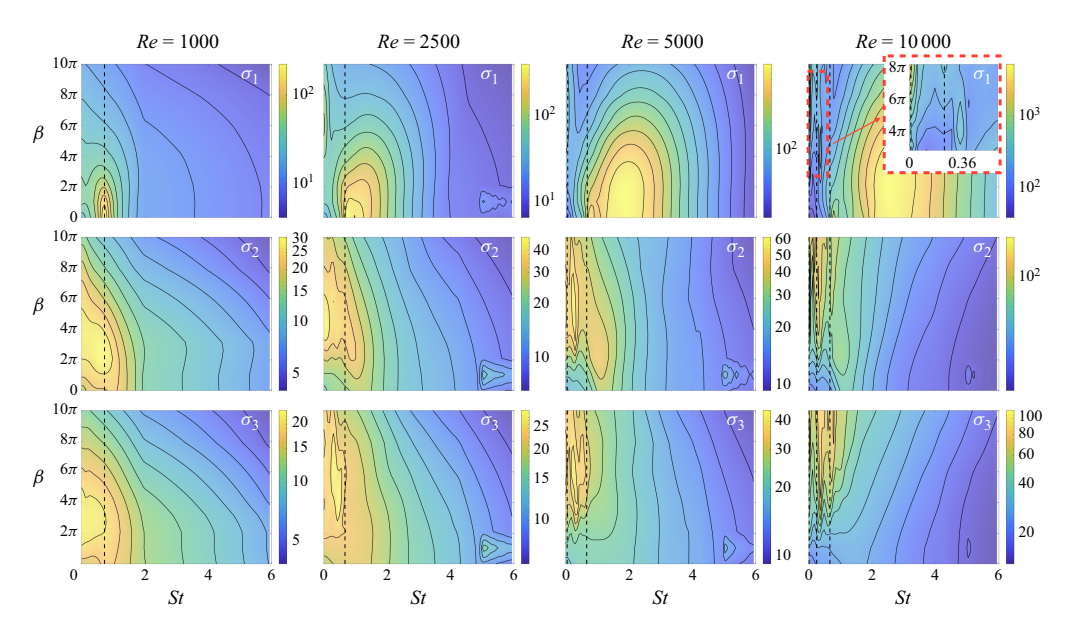


Figure 15. Gain distributions of the first three singular values over the  $\beta - St$  plane at Re = 1000, 2500, 5000 and 10 000 at  $t_{\gamma} = 2.5$ . Black dashed lines indicate the dominant frequency peaks associated with lift coefficients, see figure 5.

at short time scale reflect the relevance of finer spanwise structures, need more time to grow and overcome the energy of two-dimensional mechanisms that prevail at short time scale. At  $Re=10\,000$ , we show a zoomed-in view of the low-St and high- $\beta$  parametric space, showing the emergence of a local maximum at  $St\approx0.36$  and  $\beta\approx4\pi$ , which reflects the large real part eigenvalue presented in figure 13.

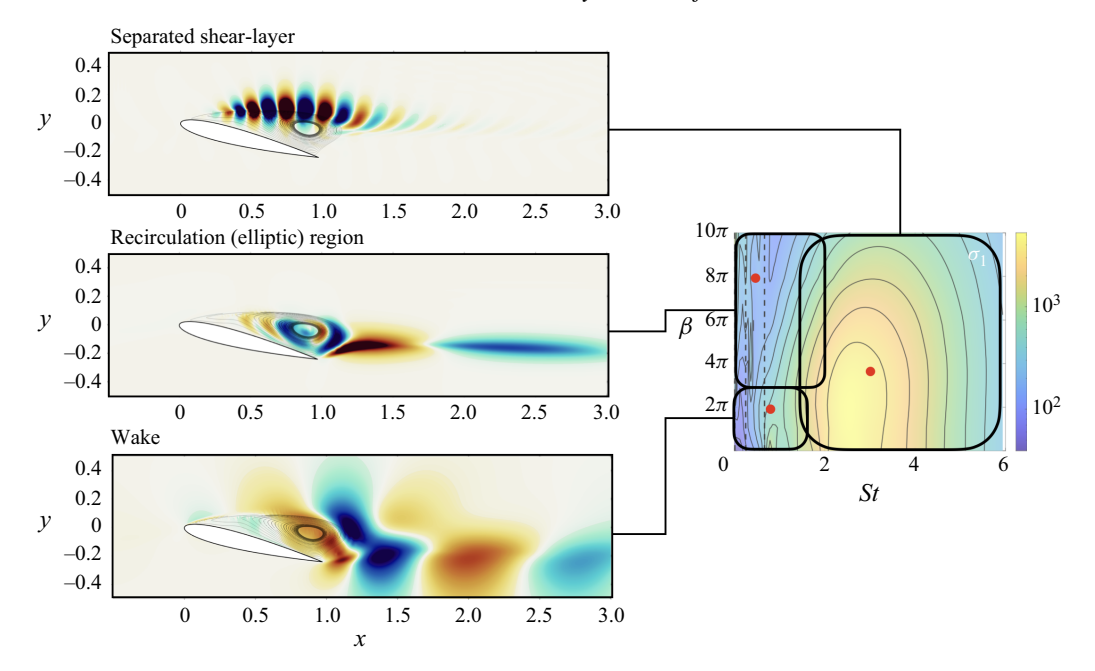


Figure 16. Response modal structures in the frequency–wavenumber space for the  $Re = 10\,000$  case at  $t_{\gamma} = 2.5$ , shown alongside the corresponding primary gain  $\sigma_1$  contour map. Shown are the vertical velocity components of selected response modes marked by the red dots, superimposed on base flow streamlines within the recirculation region.

Spanwise effects are thus seen to affect the low-frequency dynamics over long time scale. At the highest Reynolds number, we observe that the modal structures at low frequencies and high spanwise wavenumber ( $\beta$ ) predominantly affect the recirculation region, which presents elliptical streamlines. At lower  $\beta$ , the dynamics are concentrated in the wake, which was also observed for the  $\beta=0$  case in the previous section. In our analysis, elliptic instabilities emerge clearly over long time horizons, suggesting that while their growth is weak, they represent persistent, spatially localized structures in the recirculation zone. This is in contrast to higher-frequency modes, which show maximum gain near  $\beta=0$  and remain largely unaffected by the time scale. These modes are linked to shear-layer dynamics and correspond to the quasi-two-dimensional roll-up of the shear layer separating from the leading edge, as seen in figure 4(c,d).

The different frequency-wavenumber responses are summarized in figure 16. An analogous division of mechanisms was proposed by Pickering *et al.* (2020) for jet flows, associating low-frequency/low-wavenumber modes with the Orr mechanism, high-frequency modes with the Kelvin-Helmholtz instability, as in our case, and low-frequency/high-wavenumber modes with streak-like features.

High- $\beta$ , low-frequency phenomena might also be linked to bursting. Indeed, numerical simulations have shown that bursting occurs when three-dimensional disturbances in the aft part of the recirculation region grow to levels sufficient to break up the shear-layer roll-up vortices, reducing their spanwise coherence (Marxen & Henningson 2011; Toppings & Yarusevych 2024).

Previous studies at lower Reynolds numbers also report that the two-dimensional vortex shedding mechanism is predominant (He *et al.* 2017; Nastro *et al.* 2023), in agreement with the present results at Re = 1000. By increasing the Reynolds number, this is true for the

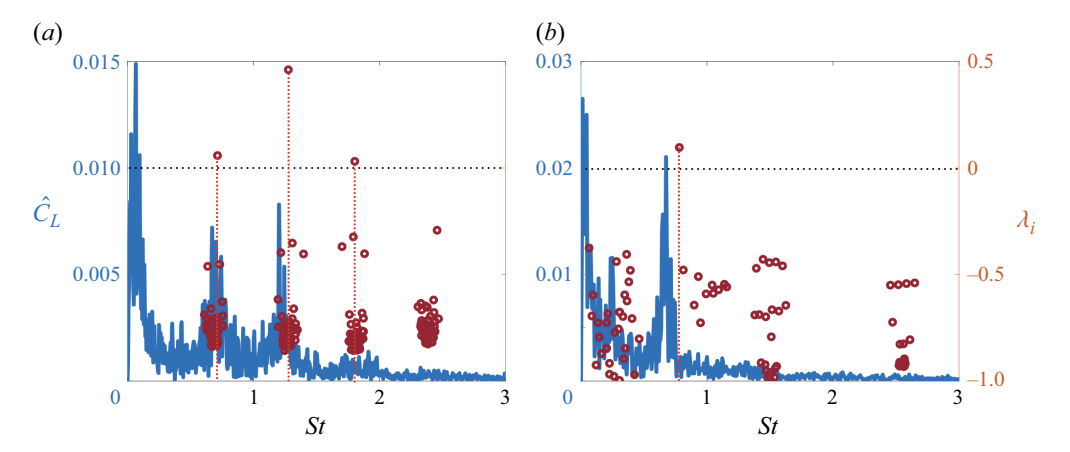


Figure 17. Lift spectra  $\hat{C}_L$  shown together with the eigenvalues for (a)  $\alpha = 9^{\circ}$  and (b) 14° at  $Re = 10\,000$ .

shear layer, which present structures with high energy gains at  $\beta = 0$ , while less energetic three-dimensional mechanisms appear at lower frequencies.

## 5. Scaling of wake and shear-layer dynamics

Up to this point, we have focused on a specific angle of attack for analysing the forcing modes, response modes and gain distributions. Let us generalize how the shear and wake dynamics relate and shift from one another across the angles of attack and Reynolds numbers. To do so, we analyse the separated flow around a NACA0012 airfoil at an angle of attack of  $\alpha = 9^{\circ}$ , and compare the results with those obtained for  $\alpha = 14^{\circ}$ . We consider the case of spanwise wavenumber  $\beta = 0$ .

The eigenvalues with the largest real component, together with the lift spectra at  $Re = 10\,000$  for the two angles of attack are shown in figure 17. At  $\alpha = 9^{\circ}$ , three eigenvalues have positive real component and reflect the peaks of the lift spectra. The largest real part of the positive eigenvalues at  $\alpha = 9^{\circ}$  is Re $\{-i\lambda\} = 0.46$ , which suggests that we consider dynamics over a time scale shorter than  $t_{\gamma} = 2.18$ . This allows us to use the discount parameter, corresponding to  $t_{\gamma} = 0.8$ , as in the previous section.

The streamwise velocity components of the first response and forcing modes are shown together with the resolvent wavemaker in figure 18, for Re = 1000 and 10 000 and the two angles of attack. The resolvent wavemaker is defined as the Hadamard, componentwise, product between forcing and response modes (Qadri & Schmid 2017; Skene *et al.* 2022):

$$\hat{\boldsymbol{w}} = \hat{\boldsymbol{f}} \circ \hat{\boldsymbol{q}}. \tag{5.1}$$

The resolvent wavemaker reveals regions that likely exhibit self-sustained mechanisms, thus regions where the response itself acts as a forcing. Let us first consider  $\alpha=14^{\circ}$ , shown in figure 18(a). At the lowest frequency, we observe differences between the two Reynolds numbers in the response, forcing and resolvent wavemaker structures. In particular, at St=0.5, we observe a thinning of the mode structures on the shear layer for the highest Reynolds number, which remains noticeable in the response mode structure up to  $St\approx 1$ . Despite this difference in the shear layer, the response modes for both cases present similarities in the wake region for Strouhal numbers  $St \leq 1$ . For higher St, the response mode structures at both the Reynolds number shift towards the shear-layer region.

## L.V. Rolandi, L. Smith, M. Amitay, V. Theofilis and K. Taira

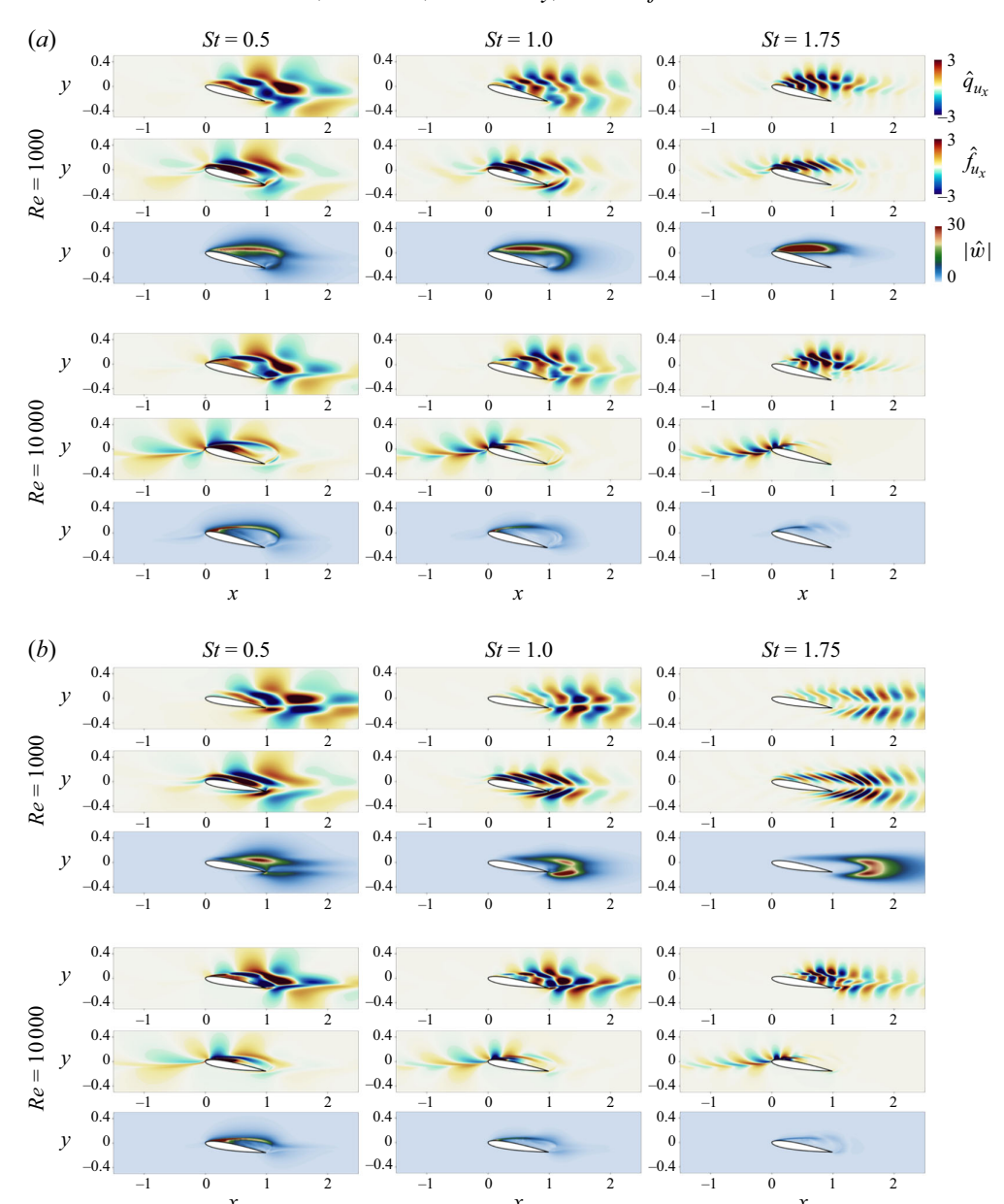


Figure 18. Streamwise velocity component of the response modes  $\hat{q}_{u_x}$ , streamwise velocity component of the forcing modes  $\hat{f}_{u_x}$  and magnitude of the wavemakers |w| shown for (a)  $\alpha=14^\circ$  and (b)  $\alpha=9^\circ$  at Reynolds numbers Re=1000 and  $10\,000$  for St=0.5, 1 and 1.75.

For the considered range of Strouhal numbers, we in contrast observe a strong difference in the forcing modes. At the highest Reynolds number the forcing mode develops upstream, as opposed to the lower Reynolds number case for which the forcing mode structures are predominant in the shear-layer region. This is also observed in the wavemaker field, which visualizes the overlap between the response and forcing modes.

For Re = 10000, we can observe again the thin elongated predominant structure over the shear layer, which weakens for higher St, as opposed to the Re = 1000 case for

which the wavemaker intensifies in the shear layer. For both Re = 1000 and  $10\,000$ , we observe that the response and forcing modes for St < 1 present structures on the wake, thus indicating wake dynamics, while for St > 1 the modes shift towards the shear-layer region, thus indicating shear-layer dynamics. The broader and more intense wavemaker region observed at Re = 1000, which reflects a stronger and wider overlap between forcing and response, highlights the region where self-sustained mechanisms are likely to be active. This is consistent with the oscillator-type behaviour, which is characterized by self-sustained vortex shedding.

The streamwise velocity component of the response and forcing modes, along with the wavemaker of the first singular mode for  $\alpha = 9^{\circ}$  at Re = 1000 and  $10\,000$ , are shown in figure 18(b). At Re = 1000, both the response and forcing modes are similar between  $\alpha = 9^{\circ}$  and 14° at low frequencies, see structures at St = 0.5, which persist up to  $St \approx 0.75$ . The structure of both cases is mainly concentrated in the downstream part of the recirculation region, with a dominating wake structure (oscillator-type). However, some differences can be seen in the wavemaker. For the  $\alpha = 9^{\circ}$ , the wavemaker vanishes close to the suction side, while this is not the case for the 14° case, for which a high magnitude of the wavemaker is present at the separation point. For higher frequencies,  $St \ge 0.75$ , the response and forcing modes of the two angles of attack are different. For  $\alpha = 9^{\circ}$ , the structures persist downstream far from the wing in the wake region but with reduced intensity. In contrast, for  $\alpha = 14^{\circ}$ , the modal structures gradually concentrate in the shear layer above the wing. The main difference between the two cases is that the unsteady flow around the airfoil is two-dimensional at  $\alpha = 9^{\circ}$  and Re = 1000, while the flow is threedimensional at  $\alpha = 14^{\circ}$  and Re = 1000. The three-dimensionality substantially modifies the shear layer above the wing, which likely causes the differences in the evolution of the modal structures, observed for the two angles of attack when increasing the frequency. Although the shear layer at  $\alpha = 14^{\circ}$  and Re = 1000 supports the modal structures, these structures are not amplified, as seen in the gain variation for  $\alpha = 14^{\circ}$  at Re = 1000.

The comparison between the resolvent modes across  $\alpha = 9^{\circ}$  and  $14^{\circ}$  at the higher Reynolds number,  $Re = 10\,000$ , also reveals similarities between the two angles of attack, but again only at the lower frequencies, up to  $St \approx 1$ . For the  $9^{\circ}$  case, the shift of the response from the wake to the shear-layer region is not as clear as for the  $14^{\circ}$  case. At  $\alpha = 9^{\circ}$  and  $St \geqslant 1$ , the modes present structures in both the wake and the shear layer. In particular, wake structures persist for higher frequencies compared with the  $14^{\circ}$  case. This is because wake dynamics are governed by the angle of attack. In fact, the wake characteristic frequency depends on the width of the wake (Roshko 1954), which becomes thinner as the angle of attack decreases and can thus support higher frequencies compared with higher angles of attack.

The gain variation of the first mode with respect to St and  $St_{\alpha}$ , where

$$St_{\alpha} = \frac{\omega c \sin \alpha}{2\pi U_{\infty}} = St \sin \alpha,$$
 (5.2)

is shown in figure 19. The figure annotates the regions of the gain distribution that correspond to wake or shear-layer dynamics. The energy amplification at  $\alpha = 9^{\circ}$  is higher compared with  $\alpha = 14^{\circ}$ , and exhibits pronounced local maximum. This is due to the eigenvalues presented in figure 17. The higher  $\lambda_i$  and multiple eigenvalues for  $\alpha = 9^{\circ}$  translate in a higher gain and multiple 'bumps' compared with the  $\alpha = 14^{\circ}$  case, due to the proximity of the integration path to the eigenvalues. In figure 19(a), we observe that the most pronounced relative peak for  $\alpha = 9^{\circ}$ , at  $St \approx 1.3$ , corresponds to the largest eigenvalues and highlights wake dynamics. This occurs at a higher frequency compared with the  $\alpha = 14^{\circ}$  local peak, around  $St \approx 0.7$ . On the contrary, for the two angles of attack,

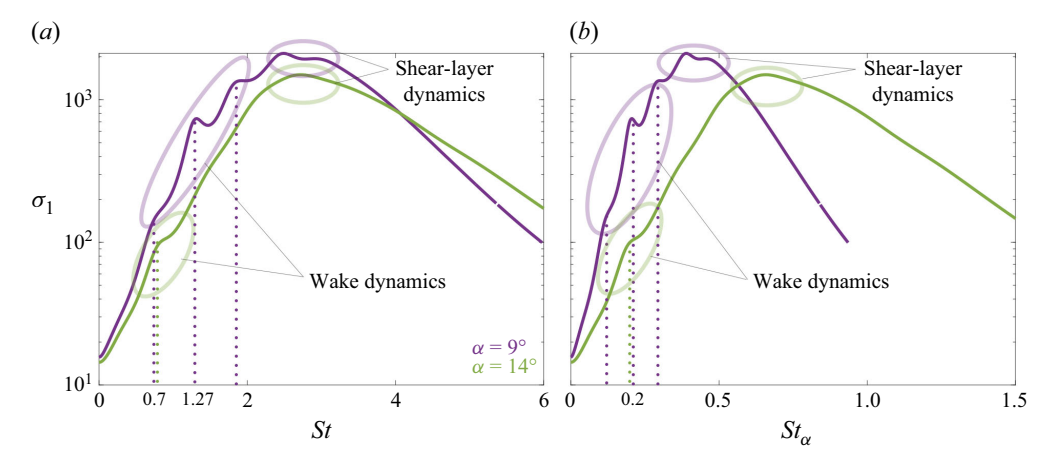


Figure 19. Gain distributions of the first mode for  $\alpha = 9^{\circ}$  and  $14^{\circ}$  at  $Re = 10\,000$  and  $t_{\gamma} = 0.8$  over (a) Strouhal number  $St_{\alpha}$  based on the front facing area. Dotted lines indicate the frequency associated with the positive eigenvalues (figure 17).

the maximum at higher frequencies, corresponding to the shear-layer dynamics, occurs at about the same frequency,  $St \approx 2.7$ .

When looking at the gain variation with respect to  $St_{\alpha}$ , figure 19(b), we observe that the wake dynamics is predominant at the same frequency for the two angles of attack. In particular, the most pronounced low-frequency peaks occur at  $St_{\alpha} \approx 0.2$  (Fage & Johansen 1927), indicating phenomena induced by the frontal wing height. However, we can see that the most energetic shear-layer dynamics at the two angles of attack does not occur at the same frequencies when considering frequencies based on the angle of attack. Moreover, in the previous section, we observed that the separated shear-layer frequency increases with the Reynolds number. These two observations highlight dynamics within the shear layer which depend on the Reynolds number but not on the angle of attack. This can be also observed in the results presented by Yeh & Taira (2019), where the flows at Reynolds number  $Re = 23\,000$  and angles of attack  $\alpha = 6^{\circ}$  and  $9^{\circ}$  are investigated. The shear dynamics was observed not to be influenced by the angle of attack, with maximum peak at  $St \approx 4.8$  for both  $\alpha$  for their cases.

When the boundary layer separates without reattaching to the airfoil, it exhibits a characteristic frequency that scales like that of a free shear layer (Ho & Huerre 1984; Kotapati *et al.* 2010). The frequency depends on the boundary layer thickness at the separation point (Bloor 1964). We show the gain variation over the normalized frequency based on the laminar boundary layer thickness  $\delta \approx 1/\sqrt{Re}$  (Bloor 1964),

$$St_{Re} = \frac{\omega c \delta}{2\pi U_{\infty}} = \frac{St}{\sqrt{Re}},$$
 (5.3)

in figure 20(a). We observe that the maximum gains occur at a similar normalized frequency. In fact, we find that the frequency of maximum gain and the corresponding streamwise characteristic length of the shear-layer dynamics occur at

$$St \approx 0.027\sqrt{Re}, \quad \lambda_x \approx 37/\sqrt{Re}.$$
 (5.4)

The value of the normalized Strouhal number is in agreement with the range of  $St/\sqrt{Re} \in [0.02, 0.03]$  proposed by Zaman & McKinzie (1991) as the range of effective excitation frequencies in acoustic control of flow over airfoils (Yarusevych, Kawall & Sullivan 2003;

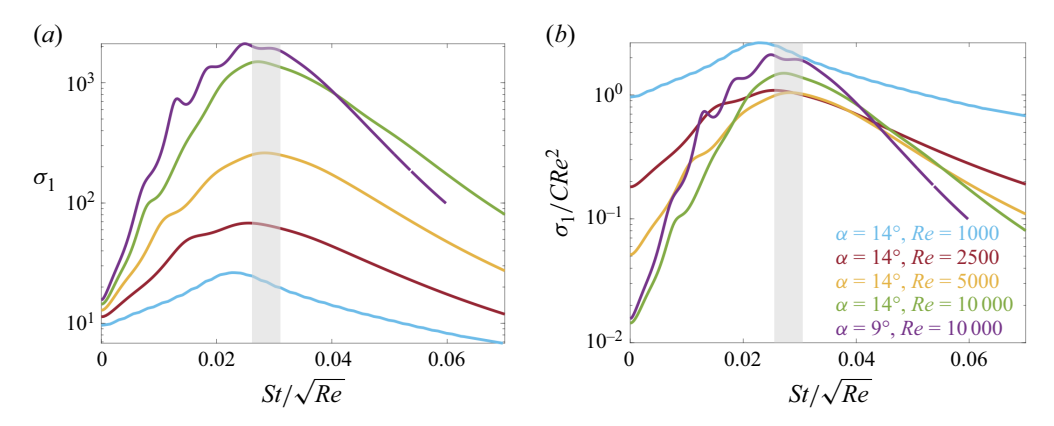


Figure 20. Gain and frequency normalization for various angles of attack and Reynolds number.

Genç et al. 2016). Ho & Huerre (1984) also report a similar value of the normalized shear-layer frequency, close to 0.03, for a laminar flow, when normalized by the momentum thickness and the average velocity across the shear layer (Ho & Huerre 1984; Kotapati et al. 2010). Results from Yeh & Taira (2019) are also in agreement with the most amplified frequency related to shear-layer dynamics  $(St/\sqrt{Re} \approx 4.8/\sqrt{23\,000} \approx 0.032)$ . Experimental results from Klewicki et al. (2024) at higher Reynolds numbers also fall in the same range  $(St/\sqrt{Re} \approx 0.021 \text{ for } Re = 2 \times 10^4 \text{ and } St/\sqrt{Re} \approx 0.027 \text{ for } Re = 4 - 8 \times 10^4)$ . Their study examines the flow around a wing of aspect-ratio of 3 with mounted walls, and the lower value of  $St/\sqrt{Re}$  at  $Re = 2 \times 10^4$  is likely due to the effects of the wall that at the lower Reynolds number cause a higher three-dimensionality of the flow and a stabilization of the shear layer at the extremes.

It is worth noticing that the Re = 1000 case does not align with the normalization. This is due to the fact that, at this Reynolds number, the dynamics (and the peak) are associated with wake dynamics rather than shear-layer ones, as discussed in § 4.2.

The energy amplification is scaled by  $Re^2$  in figure 20(*b*), showing an almost quadratic variation of the amplification energy with respect to the Reynolds number. The distributions of  $\sigma_1$  are also scaled by constant *C* that scales the peaks to be close to 1. In this case, we have used  $C = 10^{-5}$ . Previous works show the maximum gain to quadratically depend on the Reynolds number in planar flows such as plane Poiseulle, Couette flow and Blasius boundary layer (Schmid, Henningson & Jankowski 2002), but also in accelerating–decelerating flows (Linot, Schmid & Taira 2024), and oscillatory flows (Xu, Song & Avila 2021).

#### 6. Conclusions

We provided a comprehensive analysis of the behaviour of separated flows over an airfoil under spanwise homogeneous conditions. The study explored Reynolds numbers spanning one to two orders of magnitude higher than earlier work, highlighting two distinct dynamics at play and documenting their characteristic frequencies.

To do so, we employed biglobal resolvent analysis and investigated the effects of the Reynolds number Re = 1000, 2500, 5000 and 10 000 on separated flow around a NACA0012 airfoil at 14° angle of attack. To compute the base flows, we performed direct numerical simulations for Re = 1000 and 2500, and wall-resolved large eddy simulations for Re = 5000 and 10 000. At these Reynolds numbers, the flow is three-dimensional,

presenting spanwise periodic structures at Re = 1000 and 2500 whose wavelengths decrease as the Reynolds increases. The two-dimensional base flows were obtained by performing a time- and spanwise-average of the unsteady flow.

We observed that the recirculation region shortened from Re = 1000 to Re = 2500, before elongating again as the Reynolds number increases further. Additionally, for  $Re \ge 2500$ , a secondary recirculation region emerges on the suction side of the airfoil and remains present at higher Reynolds numbers. The energy spectra evaluated at four streamwise locations along the shear layer, showed high-frequency contents at specific cross-stream locations, and at higher frequencies when increasing the Reynolds number.

Our results were organized in two parts. In the first part, the results of the resolvent analysis were examined with respect to the different parameters: discount parameter, spanwise wavenumber and frequency. Varying the discount parameter allowed us to consider the dynamics over different time scales. The results showed that, at short time scales, shear-layer dynamics were the most energetic, while at longer time scales wake dynamics prevailed. Three-dimensionality, investigated by varying the spanwise wavenumber, also seemed to be effective at long time scales and to be sustained by low frequencies. At the highest Reynolds number, low-frequency and high-wavenumber modal structures were observed within the recirculation region, suggesting the presence of elliptic instability mechanisms. In contrast, the shear-layer dynamics, which occurred at higher frequencies, remained predominantly two-dimensional.

In the second part, we compared the results with a different angle of attack, still focusing on the shear-layer and wake dynamics. While wake dynamics were influenced by the angle of attack, shear-layer dynamics depended solely on the Reynolds number. The main frequencies that characterized the two different dynamics approached each other when decreasing the angle of attack at a constant Reynolds number, while they separated when increasing the Reynolds number at a constant angle of attack. Normalizing the Strouhal number by the Reynolds number  $(St/\sqrt{Re})$  highlighted the shear-layer scaling, with maximum energy amplification occurring at  $St \approx 0.027\sqrt{Re}$ , consistent with prior studies. Moreover, the energy amplification scales quadratically with Re.

This study revealed the dominant wake and shear-layer dynamics, emphasizing their dependence on the Reynolds number and angle of attack. The identified scalings and trends bridge gaps in understanding transitional flow regimes. These insights are useful for improving predictions and control strategies for flows at even higher Reynolds numbers.

**Acknowledgements.** This work used computational and storage services associated with the Hoffman2 Shared Cluster provided by UCLA Institute for Digital Research and Education's Research Technology Group. L.V.R. and K.T. thank C. Klewicki for insightful discussions.

**Funding.** This work was supported by the U.S. Army Research Office (grant no. W911NF-21-1-0060) and the U.S. Air Force Office of Scientific Research (grant no. FA9550-21-1-0174).

**Declaration of interest.** The authors report no conflict of interest.

## Appendix A. Effects of the discount parameter

In this appendix, we report further analysis on the effect of the discount parameter  $\gamma$ . In § 4.2, it has been shown that the dominance of the wake and shear-layer modes changes with  $t_{\gamma} = 1/\gamma$ . In particular, at short time scales, higher energy amplifications occur at high frequency, in the shear layer, while at long time scales, wake dynamics arising at low frequency show higher energy amplification. Figure 21 shows the energy gain of the wake and shear-layer modes, at  $St_W$  and  $St_S$ , respectively, over  $t_{\gamma}$ . The energy gain of the two modes increases over time with different slopes. In particular, we can observe that

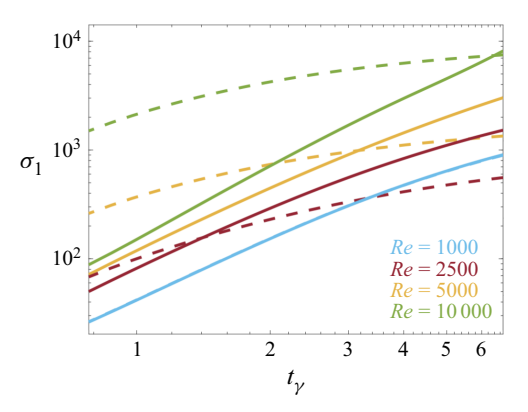


Figure 21. Variation of the first singular value  $\sigma_1$  over time  $t_{\gamma}$  at the frequencies of the maximum gain over short and long time scales. Here (——) indicates the wake mode frequency (lower frequency peak) and (- - -) indicates the shear-layer mode frequency (higher frequency peak).

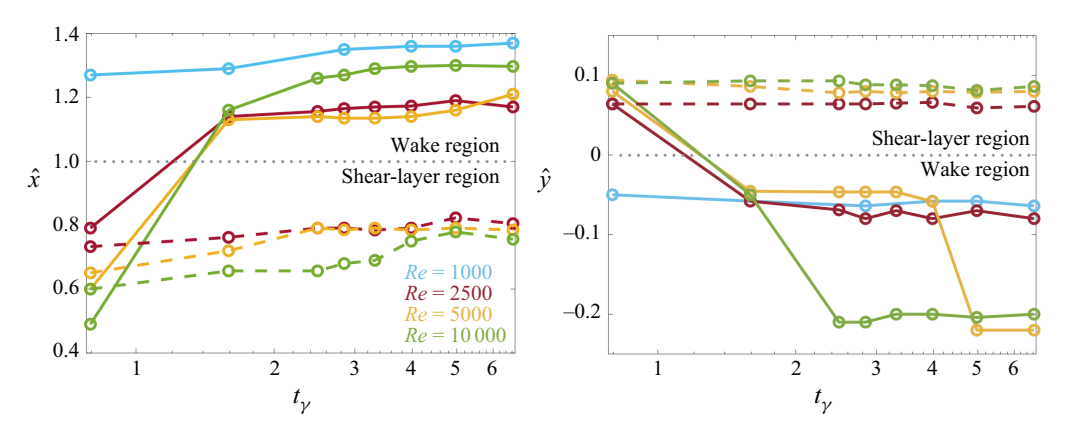


Figure 22. Streamwise and cross-stream position of the maximum kinetic energy of the shear response mode (----) and wake response mode (----) over time  $t_{\gamma}$ .

the wake mode energy increase is steeper compared with the shear-layer mode, while the shear-layer mode seems to tend towards an asymptotic plateau. From this plot, we can see that the time at which the wake mode prevails over the shear-layer mode increases with the Reynolds number.

The variation in time of the response modes can be investigated also by tracking the streamwise and cross-stream position of the maximum kinetic energy of the response mode. This is shown in figure 22, considering

$$\{\hat{x}, \, \hat{y}\} = \underset{x, \, y}{\arg \max} ||\hat{q}_{u}||_{2}(x, \, y),$$
 (A1)

where  $\hat{q}_u = (\hat{q}_{u_x}, \hat{q}_{u_y}, \hat{q}_{u_z})$ . From these plots, we observe that for the cases in which the shear layer supports energetic modal structures ( $Re \ge 2500$ ), the location of the shear-layer mode's maximum intensity remains almost unchanged. Interestingly, in these cases, the wake mode is most intense in the shear-layer region over short times before eventually shifting towards the wake region. The streamwise and cross-stream location of the shear mode and wake mode over a short time scale show good agreement with the region of high amplitude in the energy spectra contour shown in figure 7. At Re = 1000, the location

## L.V. Rolandi, L. Smith, M. Amitay, V. Theofilis and K. Taira

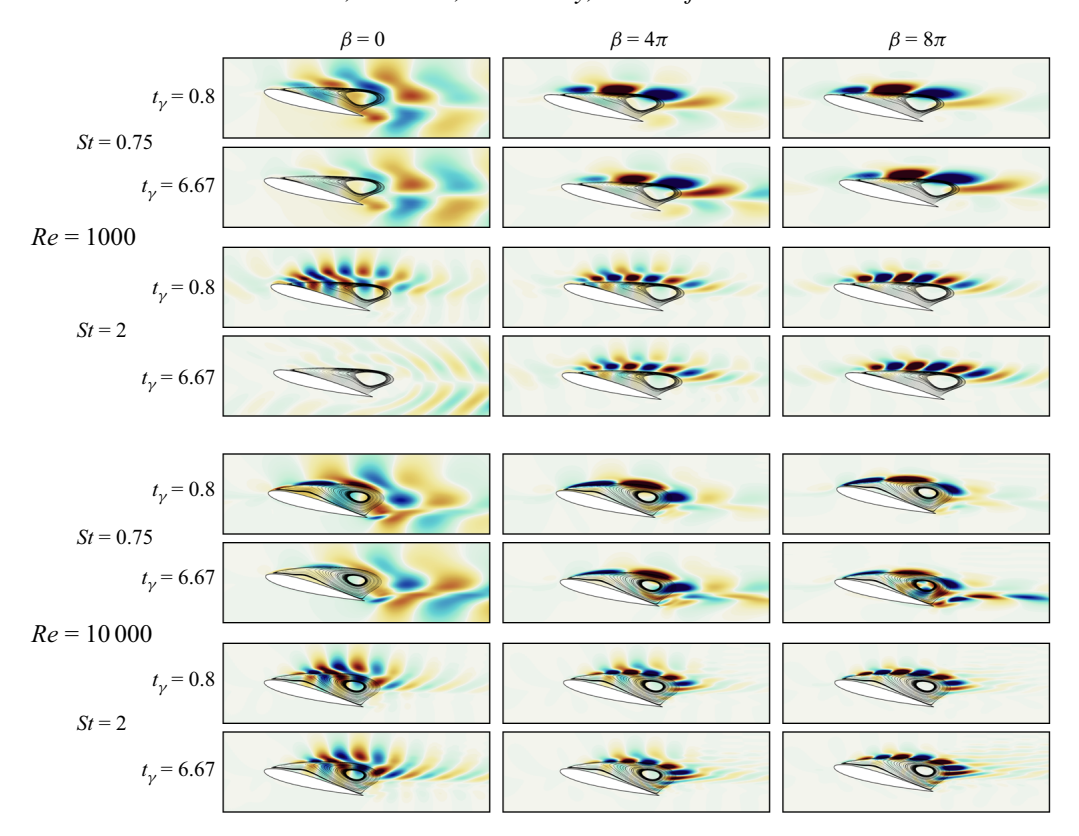


Figure 23. Streamwise velocity response contours at St = 0.75, 2 and  $\beta = 0.4\pi$  and  $8\pi$  for Re = 1000,  $10\,000$  and  $t_{\gamma} = 0.8$  and 6.67, superposed to base flow velocity streamlines within the recirculation region.

of the wake mode's maximum intensity remains almost constant over time. Additionally, the streamwise position of the wake mode at long time scales is correlated to the length of the base flow recirculation region (see figure 9e). The response mode at Re = 1000 is most intense farther downstream compared with the higher Reynolds number cases, as its recirculation region is the most elongated. Moreover, the response modes at Re = 2500 and 5000 are most intense at a similar streamwise location as their recirculation regions have comparable extensions.

## Appendix B. Spanwise wavenumber effects on the response modal structures

In § 4.3, we have presented the effects of the spanwise wavenumber  $\beta$  on the gain variation as a function of the frequency. In this appendix, we report the changes in the response modal structures with respect to  $\beta$ . The effect of  $\beta$  on the response mode structures is shown in figure 23 for Re = 1000 and 10000, at frequencies St = 0.75 and 2 and two different time scales. The streamlines of the base flow are also plotted to highlight the recirculation region.

We first consider the lower frequency, St = 0.75. Over  $t_{\gamma} = 0.8$  and at  $\beta = 0$ , the response mode structure develops in the wake region for both Reynolds numbers. The structure presents alternating oblique structures characteristic of the streamwise velocity component of oscillating modes. As  $\beta$  increases, these elongated structures gradually evolve into alternating concentrated structures located in the shear layer. This transition

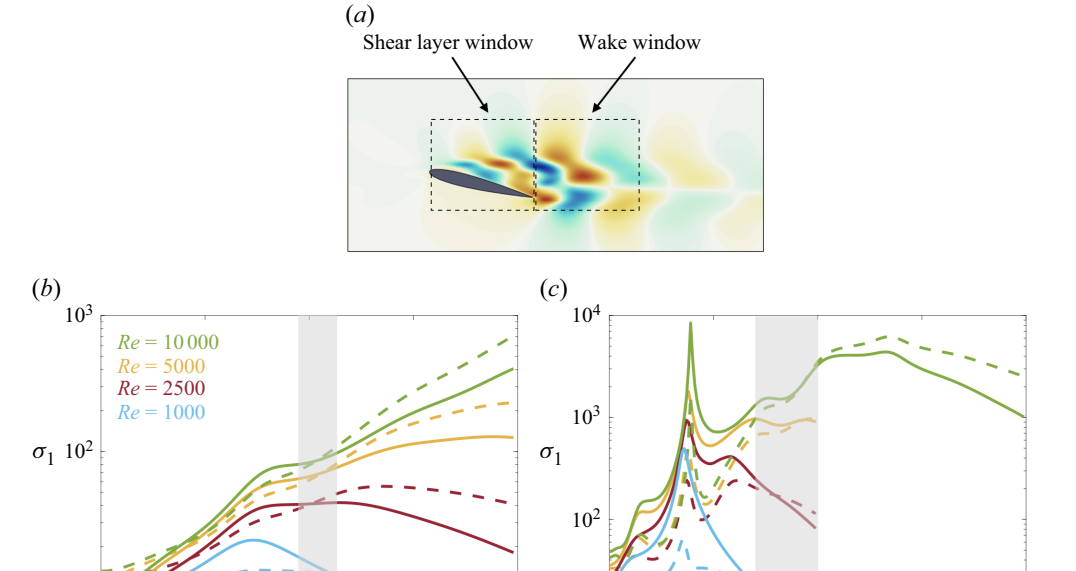


Figure 24. The domain considered for the shear layer and wake window (a), and first gain variation over frequency for wake window (——), and shear-layer window (- - - -) over short time scale  $t_{\gamma} = 0.8$  (b) and long time scale  $t_{\gamma} = 6.67$  (c). Grey bands indicate the shift between wake and separated shear-layer modes.

2.0

 $10^{1}$ 

1

2 St

occurs because smaller structures require stronger mean shear for amplification (Yeh & Taira 2019; Skene *et al.* 2022). Over  $t_{\gamma} = 6.67$  and Re = 1000, the behaviour observed over the shorter time scale persists. However, for  $t_{\gamma} = 6.67$  and  $Re = 10\,000$ , the mode becomes spatially concentrated in the recirculation (elliptic) region and the trailing edge shear-layer region at the highest  $\beta$ .

Now, let us consider the higher frequency, St = 2. Over  $t_{\gamma} = 0.8$ , the response mode for both Reynolds numbers gradually transitions from alternating oblique structures to alternating concentrated structures within the shear-layer region. Over  $t_{\gamma} = 6.67$  and at Re = 1000, a mode switching occurs and structures emerge in the shear layer for higher  $\beta$  values, which are absent at  $\beta = 0$ . Over  $t_{\gamma} = 6.67$  and at  $Re = 10\,000$  the mode structure does not significantly change compared with the short time scale.

## Appendix C. Windowed resolvent analysis

0.5

1.0

St

1.5

To further investigate the transition from wake modes to shear-layer modes, we perform windowed resolvent analysis. The forcing is allowed to act over the entire domain, while the energy is maximized by restricting the response to the shear-layer region and the wake region, as indicated in figure 24(a). The shear and wake window correspond to the regions  $(x, y) \in [0, \cos \alpha] \times [-0.3c, 0.5c]$  and  $(x, y) \in [\cos \alpha, 2\cos \alpha] \times [-0.3c, 0.5c]$ , respectively, with the origin positioned at the leading edge.

In figure 24(b) we report the first gain evolution of the wake and shear-layer windowed resolvent analysis at  $t_{\gamma} = 0.8$ . At low forcing frequencies the dynamics is governed by shear-layer mechanisms. However, at  $St \approx 0.25$  for Re = 1000 and  $St \approx 0.4$  for  $Re \geqslant 2500$ , wake mechanisms start prevailing over the shear-layer ones. This range, where the wake

3

4

## L.V. Rolandi, L. Smith, M. Amitay, V. Theofilis and K. Taira

dynamics contribution on the total gain is higher compared with the shear-layer one, corresponds to where we observe the local peaks that are the short-time effects of the wake dynamics. At  $St \approx 1$  the dynamics is again dominated by shear-layer mechanisms. Over long time scales, as shown in figure 24(b), the shift between the wake and the separated shear-layer modes occurs at higher frequencies.

#### REFERENCES

- BALAY, S. 2020 PETSc users manual (Rev. 3.13). Tech. Rep, Argonne National Lab.
- BARKLEY, D. 2006 Linear analysis of the cylinder wake mean flow. Europhys. Lett. 75 (5), 750.
- BENEDDINE, S., SIPP, D., ARNAULT, A., DANDOIS, J. & LESSHAFFT, L. 2016 Conditions for validity of mean flow stability analysis. *J. Fluid Mech.* **798**, 485–504.
- BLOOR, M.S. 1964 The transition to turbulence in the wake of a circular cylinder. *J. Fluid Mech.* **19** (2), 290–304.
- BROEREN, A. & BRAGG, M. 1998 Low-frequency flowfield unsteadiness during airfoil stall and the influence of stall type. In *16th AIAA Applied Aerodynamics Conference*. AIAA Paper 1998-2517.
- BRUNNER, C.E., KIEFER, J., HANSEN, M.O.L. & HULTMARK, M. 2021 Study of Reynolds number effects on the aerodynamics of a moderately thick airfoil using a high-pressure wind tunnel. *Exp. Fluids* **62**, 1–17.
- CHU, B.-T. 1965 On the energy transfer to small disturbances in fluid flow (Part I). *Acta Mechanica* 1 (3), 215–234.
- COUNSIL, J.N.N. & GONI BOULAMA, K. 2013 Low-Reynolds-number aerodynamic performances of the NACA 0012 and Selig–Donovan 7003 airfoils. J. Aircraft 50 (1), 204–216.
- DAWSON, S.T.M. & McKeon, B.J. 2020 Prediction of resolvent mode shapes in supersonic turbulent boundary layers. *Intl J. Heat Fluid Flow* **85** (108677).
- DEISSLER, R.G. 1969 Nonlinear decay of a disturbance in an unbounded viscous fluid. Appl. Sci. Res. 21, 393–410.
- FAGE, A. & JOHANSEN, F.C. 1927 On the flow of air behind an inclined flat plate of infinite span. *Proc. R. Soc. Lond. Ser. A, Containing Pap. Math. Phys. Character* **116** (773), 170–197.
- GENÇ, M.S., AÇIKEL, H.H., AKPOLAT, M.T., ÖZKAN, G. & KARASU, I. 2016 Acoustic control of flow over NACA 2415 airfoil at low Reynolds numbers. *J. Aerospace Engng* **29** (6), 375–420.
- GEORGE, K.J. & SUJITH, R.I. 2011 On Chu's disturbance energy. J. Sound Vibration 330 (22), 5280-5291.
- GUPTA, S., ZHAO, J., SHARMA, A., AGRAWAL, A., HOURIGAN, K. & THOMPSON, M.C. 2023 Two-and three-dimensional wake transitions of a NACA0012 airfoil. *J. Fluid Mech.* **954**, A26.
- HE, W., GIORIA, R.D.S., PÉREZ, J.M. & THEOFILIS, V. 2017 Linear instability of low Reynolds number massively separated flow around three NACA airfoils. J. Fluid Mech. 811, 701–741.
- Ho, C.-M. & HUERRE, P. 1984 Perturbed free shear layers. Annu. Rev. Fluid Mech. 16, 365-424.
- JOVANOVIC, M.R. 2004 Modeling, analysis, and control of spatially distributed systems. PhD thesis, University of California. Santa Barbara.
- JOVANOVIĆ, M.R. 2021 From bypass transition to flow control and data-driven turbulence modeling: an inputoutput viewpoint. Annu. Rev. Fluid Mech. 53 (1), 311–345.
- JOVANOVIĆ, M.R. & BAMIEH, B. 2005 Componentwise energy amplification in channel flows. J. Fluid Mech. 534, 145–183.
- KHALIGHI, Y., HAM, F., NICHOLS, J., LELE, S. & MOIN, P. 2011 Unstructured large eddy simulation for prediction of noise issued from turbulent jets in various configurations. In AIAAPaper 2011-2886.
- KLEWICKI, C., KLOSE, B.F., JACOBS, G.B. & SPEDDING, G.R. 2024 The footprint of laminar separation on a wall-bounded wing section at transitional Reynolds numbers, arXiv preprint arXiv:2411.05926.
- KOJIMA, Y., YEH, C.-A., TAIRA, K. & KAMEDA, M. 2020 Resolvent analysis on the origin of twodimensional transonic buffet. J. Fluid Mech. 885, R1.
- KOTAPATI, R.B., MITTAL, R., MARXEN, O., HAM, F., YOU, D. & CATTAFESTA, L.N. 2010 Nonlinear dynamics and synthetic-jet-based control of a canonical separated flow. *J. Fluid Mech.* **654**, 65–97.
- LINOT, A.J., SCHMID, P.J. & TAIRA, K. 2024 On the laminar solutions and stability of accelerating and decelerating channel flows. *J. Fluid Mech.* **999**, A43.
- MARTINI, E., CAVALIERI, A.V.G., JORDAN, P., TOWNE, A. & LESSHAFFT, L. 2020 Resolvent-based optimal estimation of transitional and turbulent flows. *J. Fluid Mech.* 900, A2.
- MARXEN, O. & HENNINGSON, D.S. 2011 The effect of small-amplitude convective disturbances on the size and bursting of a laminar separation bubble. *J. Fluid Mech.* **671**, 1–33.
- MCKEON, B.J. & SHARMA, A.S. 2010 A critical-layer framework for turbulent pipe flow. *J. Fluid Mech.* **658**, 336–382.

- MENEGHINI, J.R., CARMO, B.S., TSILOUFAS, S.P., GIORIA, R.D.S. & ARANHA, J.A.P. 2011 Wake instability issues: from circular cylinders to stalled airfoils. *J. Fluid. Struct.* 27 (5–6), 694–701.
- MOARREF, R., SHARMA, A.S., TROPP, J.A. & MCKEON, B.J. 2013 Model-based scaling of the streamwise energy density in high-Reynolds-number turbulent channels. *J. Fluid Mech.* **734**, 275–316.
- MUKAI, J., ENOMOTO, S. & AOYAMA, T. 2006 Large-eddy simulation of natural low-frequency flow oscillations on an airfoil near stall. In 44th AIAA Aerospace Sciences Meeting. AIAA Paper 2006-1417.
- NAKASHIMA, S., FUKAGATA, K. & LUHAR, M. 2017 Assessment of suboptimal control for turbulent skin friction reduction via resolvent analysis. *J. Fluid Mech.* 828, 496–526.
- NASTRO, G., ROBINET, J.-C., LOISEAU, J.-C., PASSAGGIA, P.-Y. & MAZELLIER, N. 2023 Global stability, sensitivity and passive control of low-Reynolds-number flows around NACA4412 swept wings. J. Fluid Mech. 957, A5.
- NOGUEIRA, P.A.S., CAVALIERI, A.V.G., HANIFI, A. & HENNINGSON, D.S. 2020 Resolvent analysis in unbounded flows: role of free-stream modes. *Theor. Comput. Fluid Dyn.* **34** (1), 163–176.
- PICKERING, E., RIGAS, G., NOGUEIRA, P.A.S., CAVALIERI, A.V.G., SCHMIDT, O.T. & COLONIUS, T. 2020 Lift-up, Kelvin–Helmholtz and Orr mechanisms in turbulent jets. *J. Fluid Mech.* **896**, A2.
- PICKERING, E., RIGAS, G., SCHMIDT, O.T., SIPP, D. & COLONIUS, T. 2021a Optimal eddy viscosity for resolvent-based models of coherent structures in turbulent jets. J. Fluid Mech. 917, A29.
- PICKERING, E., TOWNE, A., JORDAN, P. & COLONIUS, T. 2021b Resolvent-based modeling of turbulent jet noise. J. Acousti. Soc. Am. 150 (4), 2421–2433.
- PULLIAM, T.H. & VASTANO, J.A. 1993 Transition to chaos in an open unforced 2D flow. *J. Comput. Phys.* **105** (1), 133–149.
- QADRI, U.A. & SCHMID, P.J. 2017 Frequency selection mechanisms in the flow of a laminar boundary layer over a shallow cavity. *Phys. Rev. Fluids* 2 (1), 013902.
- RIBEIRO, J.H.M. & TAIRA, K. 2024 Triglobal resolvent-analysis-based control of separated flows around low-aspect-ratio wings. J. Fluid Mech. 995, A13.
- RIBEIRO, J.H.M., YEH, C.-A., ZHANG, K. & TAIRA, K. 2022 Wing sweep effects on laminar separated flows. *J. Fluid Mech.* **950**, A23.
- ROLANDI, L.V. 2021 Stability of low Reynolds number compressible flows. *PhD thesis*, Toulouse, Institut supérieur de l'aéronautique et de l'espace.
- ROLANDI, L.V., JARDIN, T., FONTANE, J., GRESSIER, J. & JOLY, L. 2022 Stability of the low Reynolds number compressible flow past a NACA0012 airfoil. AIAA J. 60 (2), 1052–1066.
- ROLANDI, L.V., RIBEIRO, J.H.M., YEH, C.-A. & TAIRA, K. 2024 An invitation to resolvent analysis. *Theor. Comput. Fluid Dyn.* **38**, 603–639.
- ROMAN, J.E., CAMPOS, C., ROMERO, E. & TOMÁS, A. 2016 SLEPc users manual. *Tech. Rep.* DSIC-II/24/02 D. Sistemes Informàtics i Computació, Universitat Politècnica de València.
- ROSENBERG, K., SYMON, S. & MCKEON, B.J. 2019 Role of parasitic modes in nonlinear closure via the resolvent feedback loop. *Phys. Rev. Fluids* **4** (5), 052601.
- ROSHKO, A. 1954 On the development of turbulent wakes from vortex streets, NASA, Tech. Rep. 1191.
- VON, S., JAKOB, G.R., SCHMIDT, O.T., JORDAN, P. & OBERLEITHNER, K. 2024 On the role of eddy viscosity in resolvent analysis of turbulent jets. *J. Fluid Mech.* 1000, A51.
- SCHMID, P.J., HENNINGSON, DAN S. & JANKOWSKI, D.F. 2002 Stability and transition in shear flows. *Appl. Math. Sci. Appl. Mech. Rev.* **142-55** (3), B57–B59.
- SCHMIDT, O.T., TOWNE, A., RIGAS, G., COLONIUS, T. & BRÈS, G.A. 2018 Spectral analysis of jet turbulence. *J. Fluid Mech.* **855**, 953–982.
- SHEARD, G.J., THOMPSON, M.C. & HOURIGAN, K. 2005a Subharmonic mechanism of the mode C instability. Phys. Fluids 17 (11), 111702.
- SHEARD, G.J., THOMPSON, M.C., HOURIGAN, K. & LEWEKE, T. 2005b The evolution of a subharmonic mode in a vortex street. *J. Fluid Mech.* **534**, 23–38.
- SKENE, C.S., YEH, C.-A., SCHMID, P.J. & TAIRA, K. 2022 Sparsifying the resolvent forcing mode via gradient-based optimisation. *J. Fluid Mech.* **944**, A52.
- SYMON, S., MADHUSUDANAN, A., ILLINGWORTH, S.J. & MARUSIC, I. 2023 Use of eddy viscosity in resolvent analysis of turbulent channel flow. *Phys. Rev. Fluids* 8 (6), 064601.
- SYMON, S., SIPP, D. & MCKEON, B.J. 2019 A tale of two airfoils: resolvent-based modelling of an oscillator versus an amplifier from an experimental mean. *J. Fluid Mech.* **881**, 51–83.
- TAMILSELVAM, P., ASZTALOS, K.J. & DAWSON, S.T. 2022 Transient growth analysis of flow over an airfoil for identifying high-amplification, spatially-localized inputs. In *AIAA SCITECH 2022 Forum*. AIAA Paper 2022-0592.
- TANG, Y., WANG, F., WANG, C., HONG, Y., YAO, Z. & TANG, X. 2021 Low-frequency oscillation characteristics of flow for NACA66 hydrofoil under critical stall condition. *Renew. Energy* 172, 983–997.

#### L.V. Rolandi, L. Smith, M. Amitay, V. Theofilis and K. Taira

- THOMAREIS, N. & PAPADAKIS, G. 2018 Resolvent analysis of separated and attached flows around an airfoil at transitional Reynolds number. *Phys. Rev. Fluids* 3 (7), 073901.
- TOPPINGS, C.E. & YARUSEVYCH, S. 2024 Laminar separation bubble formation and bursting on a finite wing. *J. Fluid Mech.* **986**, A26.
- TOWNE, A., COLONIUS, T., JORDAN, P., CAVALIERI, A.V. & BRES, G.A. 2015 Stochastic and nonlinear forcing of wavepackets in a Mach 0.9 jet. In 21st AIAA/CEAS Aeroacoustics Conference. AIAA Paper 2015-2217.
- TOWNE, A., SCHMIDT, O.T. & COLONIUS, T. 2018 Spectral proper orthogonal decomposition and its relationship to dynamic mode decomposition and resolvent analysis. *J. Fluid Mech.* **847**, 821–867.
- TREFETHEN, L.N., TREFETHEN, A.E., REDDY, S.C. & DRISCOLL, T.A. 1993 Hydrodynamic stability without eigenvalues. *Science* **261** (5121), 578–584.
- TURTON, S.E., TUCKERMAN, L.S. & BARKLEY, D. 2015 Prediction of frequencies in thermosolutal convection from mean flows. *Phys. Rev. E* **91** (4), 043009.
- VREMAN, A.W. 2004 An eddy-viscosity subgrid-scale model for turbulent shear flow: algebraic theory and applications. *Phys. Fluids* 16 (10), 3670–3681.
- XU, D., SONG, B. & AVILA, M. 2021 Non-modal transient growth of disturbances in pulsatile and oscillatory pipe flows. J. Fluid Mech. 907, R5.
- YARUSEVYCH, S., KAWALL, J.G. & SULLIVAN, P.E. 2003 Effect of acoustic excitation on airfoil performance at low Reynolds numbers. *AIAA J.* 41 (8), 1599–1601.
- YEH, C.-A., BENTON, S.I., TAIRA, K. & GARMANN, D.J. 2020 Resolvent analysis of an airfoil laminar separation bubble at Re = 500 000. *Phys. Rev. Fluids* 5 (8), 083906.
- YEH, C.-A. & TAIRA, K. 2019 Resolvent-analysis-based design of airfoil separation control. *J. Fluid Mech.* **867**, 572–610.
- ZAMAN, K.B.M.Q., MCKINZIE, D.J. & RUMSEY, C.L. 1989 A natural low-frequency oscillation of the flow over an airfoil near stalling conditions. *J. Fluid Mech.* **202**, 403–442.
- ZAMAN, K.B.M.Q. & MCKINZIE, D.J. 1991 Control of laminar separation over airfoils by acoustic excitation. *AIAA J.* 29 (7), 1075–1083.
- ZHU, W., CHEN, X. & FU, L. 2024 Resolvent analyses of incompressible turbulent channel, pipe and boundary-layer flows. *Intl J. Heat Fluid Flow* **106**, 109331.